J Low Temp Phys (2009) 157: 324–351
DOI 10.1007/s10909-009-9918-7

Fluid States of Helium Adsorbed in Nanopores

Nobuo Wada · Taku Matsushita ·
Mitsunori Hieda · Ryo Toda

Received: 12 May 2009 / Accepted: 30 June 2009 / Published online: 21 July 2009

Abstract We have studied helium adsorbed in new nanopores which have regular structures from nano-cage to three-dimensionally (3D) connected pores. Adsorption potential and layer formation of the adsorbed helium are observed by the vapor pressure for the adsorption. New paradigms of zero-D and 1D helium fluids are realized in nano-cages and nano-channels, respectively. The superfluid onsets (transitions) in the 1D and 3D nanopores show obvious dependence on the pore connections. The superfluid in the 3D pores has properties similar to the Bose-Einstein condensation of the 3D Bose atomic gas. The films of the ^{3}He gas formed in the ^{4}He preplated nanopores show the dimensional crossover depending on the pore connection: from the 2D Boltzmann gas to a 1D or 3D gas state with decreasing temperature. This gas changes to the degenerate state in each dimension at the lower temperatures. Extremely high frequency measurements of the helium adatoms on flat substrate determined the superfluid vortex parameters of the ^{4}He films, and revealed a slippage (decoupling) of the helium adatoms in the non-superfluid state.

Keywords Helium · Superfluidity · Fermi fluids · Low-dimensional quantum systems · Nanopores

1 Introduction

The lightest monoatomic molecules of ^{4}He and ^{3}He remain liquids at absolute zero temperature. At low temperatures, the bulk ^{4}He liquid shows the three-dimensional

---

N. Wada (✉) · T. Matsushita · M. Hieda
Department of Physics, Graduate School of Science, Nagoya University, Furou-chou, Chikusa-ku, Nagoya 464-8602, Japan
e-mail: nwada@cc.nagoya-u.ac.jp

R. Toda
Research Center for Low Temperature and Materials Sciences, Kyoto University, Kyoto 606-8501, Japan

(3D) superfluid transition related to the Bose-Einstein condensate. The ^{3}He liquid becomes the 3D Fermi liquid, followed by the triplet-superfluid transitions probably due to the paramagnon interaction [1]. On flat solid surfaces such as graphite and Mylar sheet, adsorbed helium atoms form fluid films on solid (nonsuperfluid) layers. Reflecting the two-dimensionality, the ^{4}He films show the 2D Kosterlitz-Thouless superfluid transition [2, 3], and the ^{3}He films set into the degenerate state with the 2D fluctuations [4]. Interactions in these fluids can be changed more variously and widely than those of the bulk liquids, from an almost free ideal gas to the Mott-Hubbard transition [5], by changing coverage (density) and substrate potentials, and preplating other adatoms.

Recently, various kinds of nanopores which have regular void structures have been synthesized. Using these nano-extreme conditions, we have studied new paradigms of zero-D and 1D helium fluids realized in nano-cages and nano-channels, respectively [6]. The helium fluid films formed in 3D nanopores were expected to have 3D properties, due to the 3D pore (film) connections [7]. We studied the possible 3D superfluid transition and BEC for the ^{4}He fluids and the 3D gas and degenerate states of the ^{3}He films [8].

In this review, formations of layers are certified in these new nanopore substrates, and these ^{4}He (Bose) and ^{3}He (Fermi) fluid films show extraordinary properties reflecting the nano-extreme conditions or high-frequency measurements. The new nanopores which have been used in those helium studies are described in Sect. 2. In the nanopores whose pore diameters are only a few times the helium atom diameter, the states of the helium adatoms (adsorption potentials, layer formations, and so on) are determined from pressure isotherms (Sect. 3). Possible quantum fluid states of ^{4}He and ^{3}He in nanocages, 2D, 1D and 3D nanopores are observed by measuring the low temperature heat capacities (Sect. 4). Superfluidity of the ^{4}He fluid films formed in 1D and 3D nanopores are found to show an explicit dependence on the pore (film) dimension, as described in Sect. 5. When a small amount of ^{3}He is adsorbed on the pore walls of the 1D and 3D nanopores preplated with ^{4}He, the ^{3}He adatoms become a Boltzmann gas at high temperatures (Sect. 6). With decreasing temperature, the gases show the dimensional crossover from 2D Boltzmann gas to 1D or 3D gases, respectively, reflecting the pore connections. The 1D and 3D gases set into the degenerate states at the lower temperatures. In Sect. 7, we describe an extremely high frequency measurement of the 2D KT superfluid transition, which gives the precise microscopic properties of the superfluid vortices. The high frequency measurements also show a slippage of helium adatoms in the non-superfluid state in addition to that of the superfluid. Finally, Sect. 8 is devoted to conclusions.

2 Nanopores with Regular Void Structures

The 2D ^{4}He superfluid onset (transition) and the 2D ^{3}He Fermi fluids have been extensively studied for the fluid films formed on flat substrates such as Mylar sheet [2] and graphite [9]. Helium fluid films can be formed on the pore walls of Vycor glasses (porous glasses) of which pores several nm in diameter are three-dimensionally and randomly connected as shown in Fig. 1. Reppy et al. [7, 10] have pointed out the

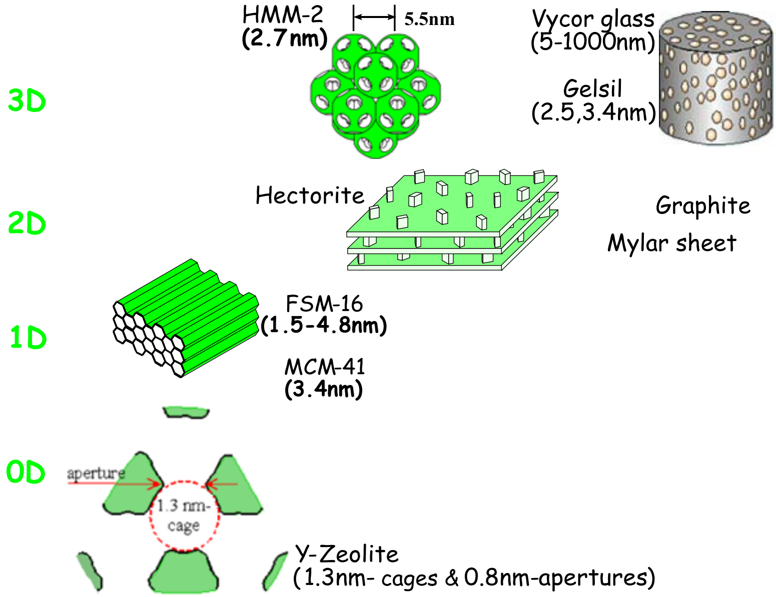

Fig. 1 (Color online) Porous substrates from three- to zero-dimensions. Pore diameters are in parentheses

possibility of the 3D superfluid transition of the ^{4}He films due to their 3D connection in the Vycor glasses. The observed superfluid properties, however, depend on the substrates even with similar pore diameters [11]. Considering the influence of the random potentials of the substrates rather than the pore connections (dimensionality), Fisher et al. alternatively proposed a Bose glass transition model [12].

Zeolites have micro-pores with regular structures whose diameters are below about 1.5 nm [13]. In the 1D micro-pores of H-ferrierite, Takaishi et al. found the 1D classical gas state of Xe at 40–120°C [14]. The adatoms are localized at the lower temperatures. The helium adatoms in the micro-pores at a full adsorption become a solid state, as indicated by the small specific heat and no obvious isotope difference. However, in Y-zeolite where cages 1.3 nm in diameter are connected through apertures of about 0.8 nm as shown in Fig. 1, the adsorbed ^{4}He and ^{3}He below the full saturation show rather large specific heat, and obvious isotope differences below about 1 K [15]. Quantum properties of the helium adatoms in the nano-cages are described in Sect. 4.1.

Recently, various kinds of nanopores have been synthesized whose pore diameters (1.5–5 nm) are between those of the typical zeolites and Vycor glasses. The nanopores have the regular pore structures from three- to one-dimensions, as shown in Fig. 1. Hectorite [16] is composed of smectite layers 0.97 nm in thickness which are separated 1.7–2 nm by pillars made of the smectite fragments. These 2D nanopores have an extremely large specific area of about 500 $\mathrm{m^2/g}$, much larger than the area ($\approx 10\ \mathrm{m^2/g}$) of graphite. FSM [17, 18] and MCM-41 [19] have honeycomb frames made of silicates. The diameter of the 1D channels can be controlled in the synthesis from about 1.5 to 5 nm. HMM-2 [20] has pores about 2.7 nm in diameter connected three-dimensionally in the period 5.5 nm with the hcp symmetry. Since these pore diameters are larger than that of zeolite, fluid states of helium adatoms are formed in the nanopores. If the dimensionality of pore connections is dominant for the ^{4}He and ^{3}He fluid properties, new helium quantum fluids in one- to three-dimensions, respectively, can be expected (Sects. 4 and 5).

Significant advantage for experimental studies is the huge specific areas of those nanopores. Practically, the small heat capacity of the ^{4}He fluid can be measured at very low temperatures by the ordinary method (Sect. 4.2).

3 Adsorption Potential and Layer Formation of Helium on Nanopore Walls

3.1 Specific Area and Pore Diameter of Nanopores

The regular structure of each nanopore has been determined by the X-ray diffraction, which precisely determines the symmetry and periodicity.

Specific areas of the substrates are usually estimated by fitting the N_2 pressure isotherms at 77 K to the Brunauer-Emmett-Teller (BET) equation. For Hectorite [21] and FSM with large diameter of about 4.7 nm, the data are well fitted to the BET equation between 0.05 and 0.3 of the saturated pressure which is the same pressure region as for the usual flat substrates. For the smaller diameter pores, fitting to the BET equation is possible only for the data in the smaller pressure region. It causes an uncertainty of the specific area for the nanopores around 2–3 nm in diameter.

The pore size distribution in the nanopores is determined from the N_2 pressure isotherm by available methods. In this paper, the pore diameter is determined by the Barrett-Joyner-Halenda (BJH) method [22]. The pore diameter estimated by the Density Functional Theory (DFT) is larger than that by the BJH method for the small pore sizes of FSM [23].

3.2 Adsorption Potential for Helium on Pore Walls

So as to first understand how helium atoms are adsorbed in the new nanopores, we studied the adsorption potential on the pore walls, layer promotions, etc. from the thermodynamic analysis of the vapor pressure for the adsorption [24].

From the temperature dependence of the pressure P at a coverage n, the work function to bring the helium adatom to the gas state (the isosteric heat of sorption) q_{st} is given by

$$q_{\mathrm{st}}(T) = -R\left[\frac{\partial \ln P}{\partial(1/T)}\right]_n . \tag{1}$$

Applying the first law of thermodynamics to an ideal gas and the adatoms, $q_{\mathrm{st}}(T) = \frac{5}{2}RT - \frac{\partial U_s(T)}{\partial n}$, where $\frac{\partial U_s(T)}{\partial n}$ is the differential molar internal energy of the adatoms. $q_{\mathrm{st}}(T)$ from the pressure data can be obtained only above about 7% of $q_{\mathrm{st}}(T)/R$ below which the vapor pressure P for the adsorption becomes negligibly small. At the lower temperatures, $\frac{\partial U_s(T)}{\partial n}$ is obtained from the heat capacity by $\frac{\partial U_s(T)}{\partial n} = -\frac{\partial U_s(0\ \mathrm{K})}{\partial n} + \int \frac{\partial C(T')}{\partial n} dT'$, where $-\frac{\partial U_s(0\ \mathrm{K})}{\partial n}$ $(= q_{\mathrm{st}}(0\ \mathrm{K}))$ is determined so that $q_{\mathrm{st}}(T)$ agrees with that obtained from the pressure data.

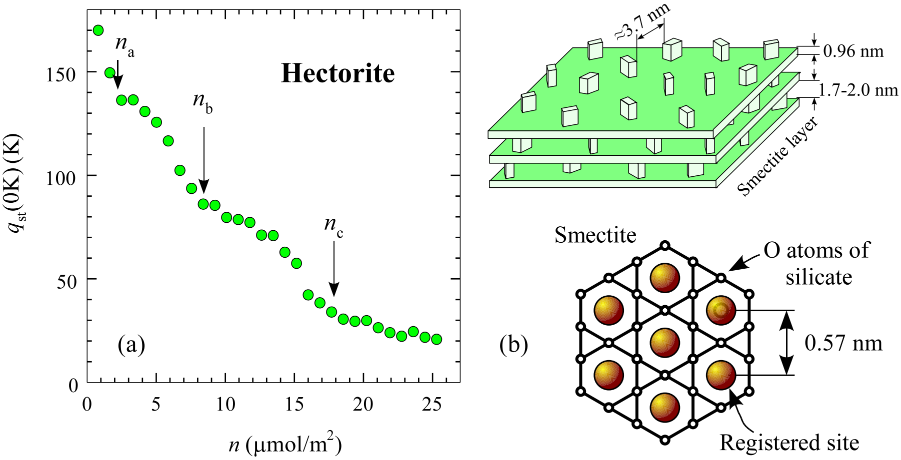

Fig. 2 (Color online) (**a**) Isosteric heat of sorption $q_{st}(0\,\mathrm{K})$ vs. coverage n of ^{4}He adsorbed in Hectorite (OH02). n_a: localization at registered sites with Na$^+$ cations, n_b: localization at all registered sites as shown in (**b**), and n_c: the first layer completion. (**b**) Surface of smectite layer of Hectorite. There are potential minima in dips (registered sites)

The frame of Y-zeolite shown in Fig. 1 is made of aluminosilicate whose charges due to $(AlO_2)^-$ are canceled by cations. Some cations appear on the pore walls, and induce localization potentials near the cations and $(AlO_2)^-$ by the electric dipole fields [25]. From $q_{st}(0\,\mathrm{K})$ for ^{4}He adsorbed in Na-Y zeolite, the localization potential by Na$^+$ and $(AlO_2)^-$ has the depth about 35 K compared with the potential ($\sim$ 160 K) on other pore walls of the aluminosilicate [26]. The localization potential can be changed by the cation size and valence charge.

Figure 2(a) shows coverage n dependence of $q_{st}(0\,\mathrm{K}) = -\frac{\partial U_s(0\ \mathrm{K})}{\partial n}$ of ^{4}He adsorbed in Hectorite (OH-02) [21]. $q_{st}(0\,\mathrm{K})$ shows the stepwise changes at $n_a = 2.2 \pm 0.5$, $n_b = 8.5 \pm 1$, and $n_c = 18 \pm 1.5$ μmol/m^2, respectively. The 2D pores of Hectorite are composed of smectite layers of which each surface is the *Kagomé* lattice of oxygen atoms of silicates, as shown in Fig. 2(b). The potential on the surface has minima at the dips (registered sites) surrounded by six oxygen atoms. Up to the coverage n_a, a helium atom is adsorbed in a dip where there is a large adsorption potential of about $-q_{st}(0\,\mathrm{K}) = -170$ K induced by a NH_4^+ cation in the bottom. At n_b, other dips without the cations localize helium atoms at -130 K. Above n_b, the helium atoms are adsorbed on the oxygen atoms of silicate with -84 K. The first layer is completed at n_c, and the second layer promotion begins at the energy -30 K. n_c is equal to the first layer coverage 19.1 μmol/m^2 of graphite within the uncertainty. The observed localization potentials on the smectite layer are likely to influence the fluid properties of the helium films, as described in Sects. 4.2 and 6.1.

In the cases of FSM [27] and HMM-2 [28], $q_{st}(T)$ of ^{4}He at low coverage is almost the same at about 110 K at $T \approx 8$ K (≈ 85 K at $T = 0$ K). Since FSM is mainly made of silicate, these pore walls are likely to be made of oxygen atoms of the silicate without a large localization site. The adsorption energy is also equal to that on the oxygen atoms of the frame of the smectite layers forming Hectorite [21].

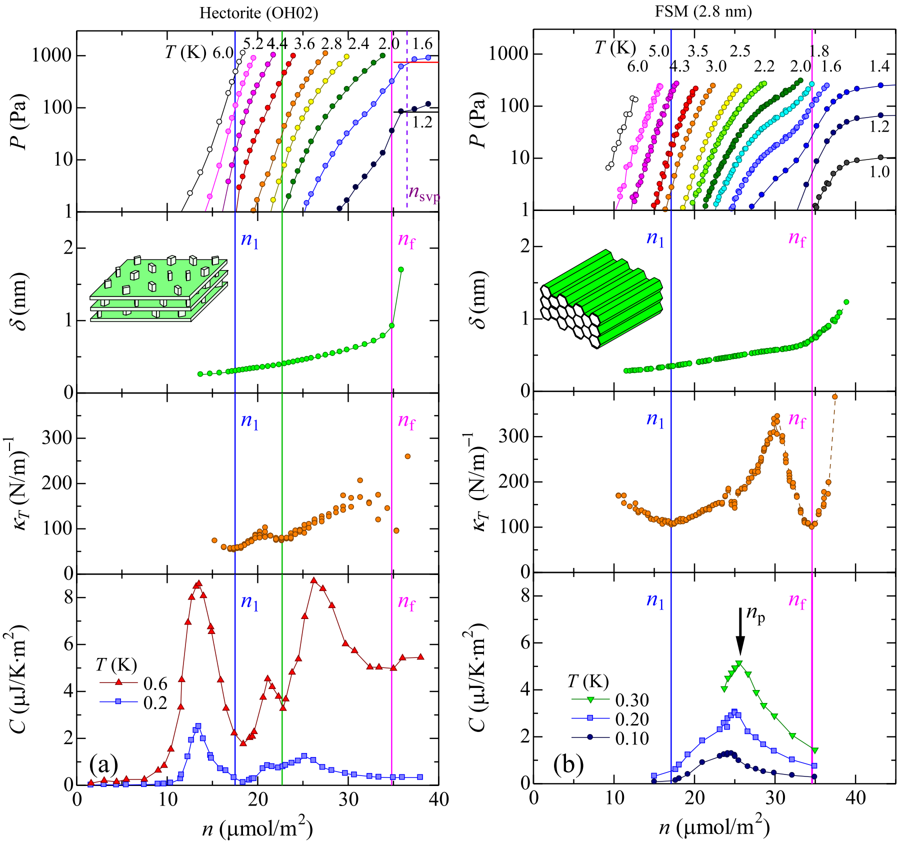

Fig. 3 (Color online) Pressure P isotherms, effective film thicknesses δ, isothermal compressibilities κ_T and heat capacity C isotherms of ^{4}He adsorbed in 2D nanopores of Hectorite (OH02) (**a**) and 1D (2.8 nm) pores of FSM (**b**), respectively. n_1 is the first layer completion, and uniform layers are formed up to n_f on the nanopore walls (see the text)

3.3 Layer Formations of Helium on Nanopore Walls

In addition to the adsorption energy q_st, the layer formation on the nanopore walls is well evaluated from the pressure isotherms by the following thermodynamic analysis [24, 29].

The P–n isotherms of ^{4}He adsorbed in Hectorite [30] and FSM (2.8 nm) [27] are shown in the tops of Figs. 3(a) and (b), respectively. The saturated vapor pressure P_0 above the coverage n_SVP indicates the full adsorption. In the Frenkel-Halsey-Hill (FHH) model, the chemical potential μ_S of the adatoms is approximately the sum of the chemical potential of the bulk liquid and the substrate adsorption potential, $-\Gamma/\delta^3$, where Γ is a constant of 1.1 K·nm^3 for the usual glass substrate and δ is the film thickness. Since μ_S is equal to the chemical potential of the gas phase which is the same as that of the ideal gas at low pressures, the effective film thickness δ of the adatoms is calculated from P of the gas phase by using

$$\delta = \left(\frac{T}{\Gamma} \ln \frac{P_0}{P}\right)^{-1/3}. \tag{2}$$

Note that this relation is strictly valid only for very thick films. However, it well describes a uniform film growth by the effective film thickness δ increasing in proportion to n up to n_f (Figs. 3(a) and (b)). Above n_f, steep increase of δ indicates the inhomogeneous adsorption.

Small deviation from the linear dependence of δ on n is shown by the isothermal compressibility κ_T defined as

$$\kappa_T = S/(n^2 RT)[\partial \ln P/\partial n]_T^{-1}, \tag{3}$$

where S is the adsorption area. κ_T shown in Fig. 3(a) and (b) shows a minimum at n_1, which indicates the first layer completion. Second layer promotion on the first layer causes the increase of κ_T above n_1. Heat capacity isotherms indicate the first layer completion at the minimum (Hectorite) and the large increment (FSM) by the second layer promotions, as shown in the bottom panels in Figs. 3(a) and (b). From δ and κ_T, a uniform layer is formed up to ($n_\mathrm{f}/n_1 =$) 2 layers in the 2D pore of Hectorite (OH-02) and 1.9 layers in the 1D (2.8 nm) pore of FSM-16.

4 Realization of Fluid Films on Nanopore Walls

4.1 Possible Helium Quantum Fluids Formed in 1.3 nm-Cages of Na-Y Zeolite

In the case of the micro-pores of Na-Y zeolite where the 1.3 nm-cages are connected through the 0.8 nm-apertures [15], the pressure isotherm of ^{4}He does not indicate the layer formations by means of the FHH model (Sect. 3.3), but shows filling of the micro-pores with ^{4}He at $n_\mathrm{SVP} \approx 27.5$ atoms/cage above which P steeply increases with n [31]. This pressure isotherm is due to the small diameter (0.8 nm) of the apertures.

Fluid states of the helium adatoms in the Na-Y zeolite were studied by measuring the heat capacity C of ^{4}He and ^{3}He at low temperatures [15, 32]. From the heat capacity data, C isotherms are obtained as shown in Fig. 4 [33].

The small heat capacities of ^{4}He and ^{3}He up to 5 atoms/cage indicates that adatoms are localized on the Na$^+$-cation sites with the potential depth 35 K (Sect. 3.2). The heat capacity becomes small again at $n_1 = 10.3$ atoms/cage (^{4}He) (10 atoms/cage (^{3}He)). This small heat capacity indicates the first layer completion at n_1 in a solid like state. Considering the void structure, the first solid layer about 0.3 nm in thickness reduces the 0.8 nm apertures to less than the helium atomic size (≈ 0.35 nm), and it covers the walls of the 1.3 nm-cage reducing it to a void of 0.7 nm diameter.

Above n_1, the adatoms promoted on the first layer have the large differential heat capacity $\partial C/\partial n$ of the order of $R/2$ at $T \gtrsim 1$ K [31]. At $11 \lessapprox n \lessapprox 18$ atoms/cage

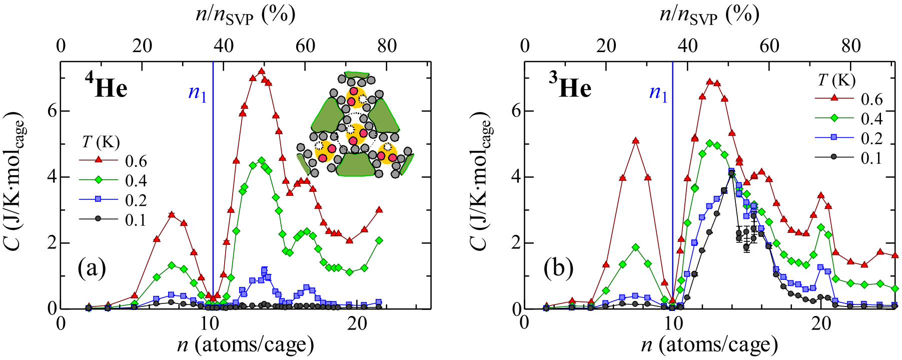

Fig. 4 (Color online) Heat capacity C isotherms of ^{4}He (**a**) and ^{3}He (**b**) adsorbed in nano-cages of Na-Y zeolite. Qualitatively different heat capacities above n_1 at low temperatures suggest that a few atoms in each cage form a quantum fluid cluster, as shown in the inset (see the text)

(40–65% of full adsorption n_{SVP}), the heat capacities of ^{3}He at the lowest temperature of $T = 0.1$ K are much larger than that of ^{4}He (Figs. 4(a) and (b)) [32]. The extremely different heat capacities at the low temperatures obviously indicate quantum-statistical differences between ^{3}He and ^{4}He adatoms. The quantum fluid states of ^{4}He as well as ^{3}He of the second layer atoms are likely to be confined in each 0.7 nm diameter void as shown in the inset of Fig. 4(a). The C-isotherms of ^{4}He have maxima at 13.5 and 17.0 atoms/cage. Between the two coverages, the second layer ^{4}He atoms are expected to be in a quantum fluid state under the Bose statistics [32]. This possible quantum region was determined up to about 1 K.

Near the full adsorption (n_{SVP}), the heat capacities become small, which shows that all of the helium adatoms become a solid state in this micro-pore.

4.2 Liquid Layers Formed in 2D Nanopores of Hectorite

2D properties of helium have been extensively studied for the substrate of graphite [9]. The phase diagrams (states) precisely determined for ^{4}He, ^{3}He and ^{3}He on ^{4}He-preplated graphite strongly reflect the potential profile on the surface [34] as well as the helium coverages [5]. On the surface of graphite, the carbon atoms form a hexagonal lattice with the period 0.142 nm.

On the smectite layer of Hectorite (Fig. 2(b)), the potential profile is completely different from that on graphite (Sect. 3.3). We studied the states of ^{4}He and ^{3}He adsorbed on Hectorite (OH02) measuring the heat capacity [21]. Note that even small specific heat of the ^{4}He adatoms at low temperatures can be measured experimentally, because of the large specific area 592 m^2/g which is about 50 times larger than ∼10 m^2/g of graphite.

Figure 5(a) and (b) show the heat capacity C isotherms of ^{4}He and ^{3}He, respectively. The small heat capacity below about 10 μmol/m^2 corresponds to the localization of the adatoms at the registered sites on the smectite surface shown in Fig. 2(b). The minimum at n_1 =18.4 μmol/m^2 for ^{4}He (16.2 μmol/m^2 for ^{3}He) is the first layer completion which is equal to n_c of q_{st} in Fig. 2(a). (The first layer coverage on graphite is 19.1 μmol/m^2.) Up to 1.4n_1, both ^{4}He and ^{3}He C-isotherms show the

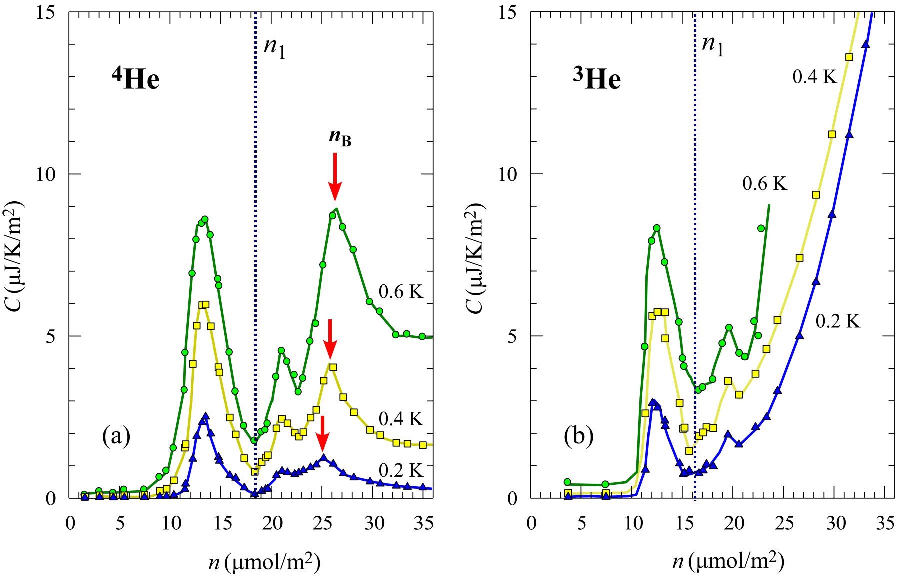

Fig. 5 (Color online) Heat capacity isotherms of ^{4}He (**a**) and ^{3}He (**b**) adsorbed on 2D nanopores of Hectorite (OH02). Quantum fluid layers appear above $1.4n_1$. Peak coverage n_B in (**a**) suggests the boundary for the Bose fluid (B) region

same coverage dependence, which indicates no quantum fluid state. Completely different isotherms are observed above about $1.4n_1$. Steep increase of the C-isotherm of ^{3}He shows the large specific heat ($\partial C/\partial n$) of the order of that in the bulk ^{3}He Fermi liquid. The C-isotherm of ^{4}He shows a characteristic peak at n_B (Fig. 5(a)) above which we can expect BEC or superfluid. We refer to this Bose quantum fluid region as the (B)-phase. The completely different heat capacities near the full adsorptions (n_{SVP}) indicate the quantum fluid states, in contrast to the solid states in the micro-pores of Na-Y zeolite near n_{SVP} (Fig. 4).

To study the ^{4}He fluid layers formed above 23 μmol/m^2, temperature dependences of the heat capacity were measured as shown in Fig. 6(a) [21]. It shows the T^2-dependence of the heat capacity below 0.2–0.3 K due to the 2D thermal phonon excitations. The low temperature heat capacity can be well fitted by $C = \gamma T + \beta T^2 + C_{2\mathrm{Droton}}$, where we assume the sum of a small heat capacity of the nonsuperfluid layers described as γT, the 2D phonon heat capacity and the 2D roton heat capacity with the gap Δ [21]. Coverage dependences of β and Δ are shown in Fig. 6(b). The large coverage dependence of βT^2-term suggests the 2D phonon heat capacity of the ^{4}He fluid layers. Thus, ^{4}He adsorbed in Hectorite show the properties of the 2D Bose liquids, reflecting the 2D pore geometry.

β of the 2D phonon heat capacity (Fig. 6(b)) gives the phonon velocity as $v_C = \sqrt{\frac{3\zeta(3)Sk_B^3}{\pi\hbar^2\beta}}$, where $\zeta(3)$ is the Riemann zeta function and S the 2D area. v_C is also described as $v_C = 1/\sqrt{\kappa_S\rho^*}$, where κ_S is the adiabatic compressibility of the 2D fluid layer and ρ^* is the fluid layer mass density. From the pressure isotherms (Fig. 3(a)), and assuming the fluid layer above the coverage $n_2 = 22.7 \pm 0.5$ μmol/m^2,

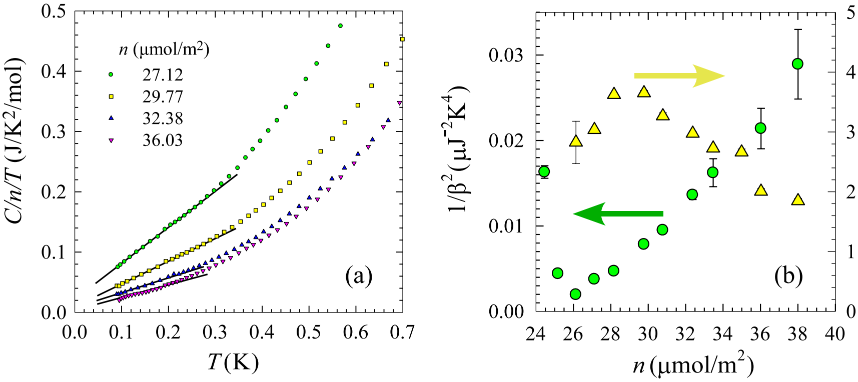

Fig. 6 (Color online) (**a**) 2D phonon heat capacity ($C/T = \beta T$) and roton one ($C \propto \exp(-\Delta/k_B T)$ of ^{4}He fluid films adsorbed in 2D nanopores of Hectorite (OH02). (**b**) Coefficient (β) of 2D phonon heat capacity and roton gap (Δ)

we can calculate the isothermal compressibility of the 2D fluid layer to be $\kappa_T^* = \frac{1}{(n-n_2)k_B T}(\frac{\partial n}{\partial \ln P})_T$. The ratio $\gamma = \kappa_T^*/\kappa_S$ is between 1 and 2. The phonon velocity v_P was also calculated from κ_T^* by using $v_P = \sqrt{\gamma/(\kappa_T^* \rho^*)}$ and assuming $\gamma \sim 1$ [30]. v_P reasonably agrees with v_C obtained from the 2D phonon heat capacity.

The 2D nanopores of Hectorite have an open spacing of 1.7–2.0 nm between the smectite layers. Uniform ^{4}He layer formation up to $n_f = 35$ µmol/m^2 is indicated by δ vs. n in Fig. 3(a). Corresponding to the increase of the fluid density with n, β and the gap energy Δ decreases above about 29 µmol/m^2 up to n_f (Fig. 6(b)). For the 2D nanopores of Hectorite, a theoretical calculation [35] suggests a puddling and capillary condensation of the ^{4}He liquid and the phonon and roton dispersions. The roton gap and other quasi-particle excitations in the ^{4}He liquid layers have been observed for rather thick films (about four atomic layers) formed on graphite by the neutron scattering studies [36].

In the 2D nanopores of Hectorite, the ^{3}He fluid layers appear above about 1.4 layers. When the 2D pore walls are preplated with 24.7 µmol/m^2 of ^{4}He and adsorbed ^{3}He at a coverage where mean atomic distance is comparable to that of bulk liquid, low temperature heat capacity of the 2D ^{3}He liquid deviates considerably from the expected linearity [37]. The deviation was accounted to large spin fluctuations characteristic to the 2D Fermi liquid [4]. The wave vector (q)-dependent spin susceptibility χ_q^0 of a degenerated Fermi gas depends on the dimensionality [38]. In the Stoner model, the spin susceptibility χ_q of a Fermi liquid with a on-site (hard core) repulsive interaction is described as $\chi_q = \chi_q^0/(1 - I\chi_q^0)$, where $I > 0$. In the 3D Fermi liquid, χ_q is enhanced at $q \approx 0$, because χ_q^0 of the 3D gas has the maximum at $q = 0$. This spin susceptibility explains the paramagnon (ferromagnetic) interaction actually observed in the 3D bulk ^{3}He Fermi liquid [1]. While χ_q^0 in the 2D Fermi gas has a maximum constant value at $q \le 2q_F$, where q_F is the Fermi wave vector. The 2D spin susceptibility χ_q enhanced at all wave vectors below $2q_F$ explains the considerable deviation from the T-linear heat capacity observed for the 2D ^{3}He Fermi liquids

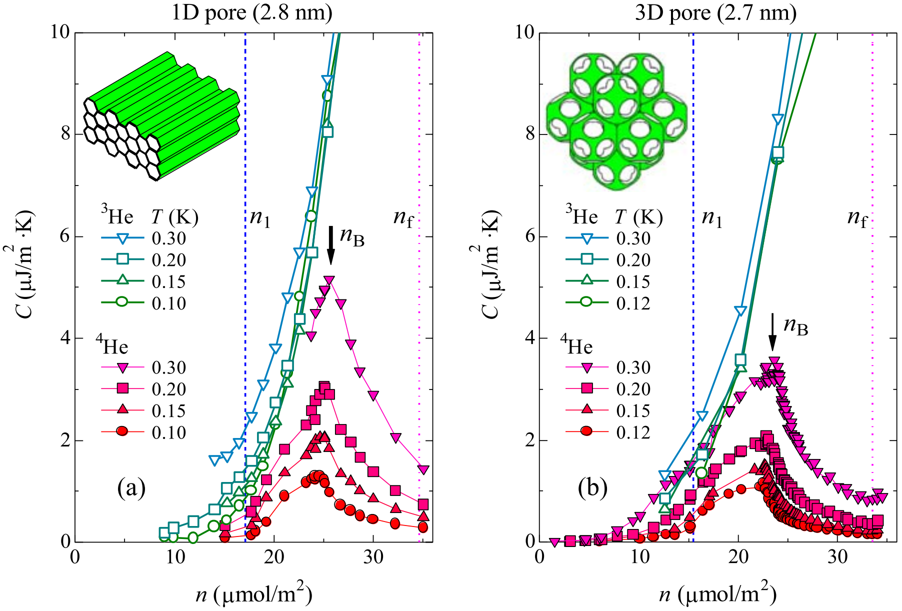

Fig. 7 (Color online) Heat capacity isotherms of ^{4}He and ^{3}He adsorbed in (**a**) 1D (2.8 nm) pores of FSM-16 and in (**b**) 3D (2.7 nm) pores of HMM-2. Peak of ^{4}He isotherm at n_B indicates the boundary of (B)-phase where BEC and superfluid are expected. The first layer is completed at n_1. Uniform layer on the nanopore walls is formed up to n_f

formed on graphite as well as Hectorite [4]. The kind of the 2D spin fluctuation is obviously different from the 3D paramagnon only at $q \approx 0$.

4.3 Fluid Films Formed in FSM (1D) and HMM-2 (3D) Nanopores

The study of the vapor pressure for the adsorption (Sect. 3) indicates that FSM (1D pore) and HMM-2 (3D pore) with the same pore diameters have similar adsorption potential profiles on the nanopore walls and the uniform layer formation of helium up to about 2 atomic layers [28]. To examine the fluid nanotubes and the fluid films with the 3D connections, respectively, we measured the heat capacities of ^{4}He and ^{3}He adsorbed in these nanopores [8].

Figure 7(a) and (b) show the heat capacity isotherms of ^{4}He and ^{3}He adsorbed in the 1D and 3D nanopores, respectively. Below n_1, both ^{4}He and ^{3}He heat capacities are small at the low temperatures. With increasing T, the heat capacity shows a cusp at T_L, as shown in Fig. 8(a) for ^{4}He in HMM-2. T_L is likely to indicate the crossover to the localized state, (L)-phase, at the lower temperatures. The phase diagram was determined as shown in Fig. 8(b). The ^{3}He heat capacity determine the same T_L vs. n diagram, except that T_L is a little (a few %) lower than that of ^{4}He. This indicates there is no quantum fluid state of the first layer.

Above about 1.4 n_1, the isotherms are completely different between ^{4}He and ^{3}He (Fig. 7(a) and (b)). The large $\frac{\partial C}{\partial n}$ of ^{3}He suggests the degenerate state of the Fermi fluid at low temperatures. The ^{4}He isotherm shows a maximum at n_B above which

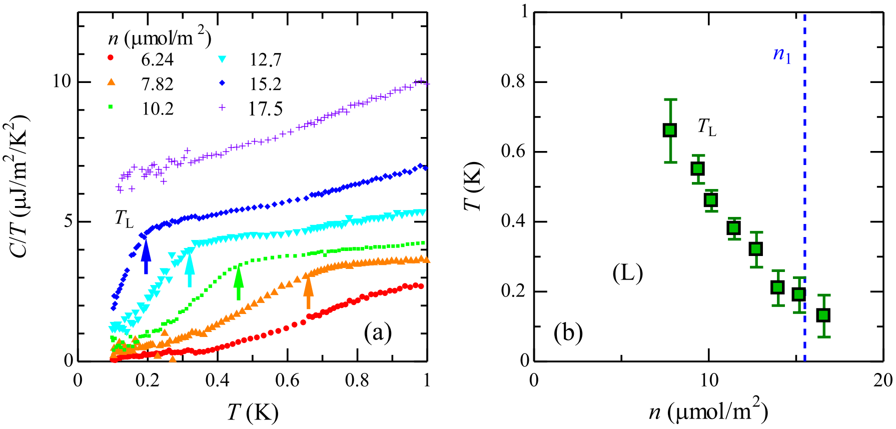

Fig. 8 (Color online) (**a**) Heat capacity of ^{4}He adsorbed in HMM-2 at low coverages below n_1. Localization state of adatoms below T_L is suggested by a steep decrease of C/T with decreasing T. (**b**) Phase diagram for the localization (L) state of ^{4}He in HMM-2

C decreases with increasing n (Fig. 7(a) and (b)). We call the region above n_B the (B)-phase, where the BEC and/or the superfluid are expected. The temperature dependences of ^{4}He adsorbed in FSM and HMM-2 are shown in Fig. 9(a) and Fig. 10(a), respectively. Each C/T shows a rounded cusp (Fig. 9(a)) or a kink (Fig. 10(a)) at T_C as marked with an arrow. From n_B and T_C, we obtained phase diagrams for the (B)-phase as shown in Fig. 11(a) and (b).

The temperature dependence in the (B)-phase (Fig. 9(a) and Fig. 10(a)) at low temperatures was analyzed by a phonon model for each pore (fluid film) geometry [39, 40]. In the case of the 2.8 nm 1D nanopores (FSM) (Fig. 9(b)), the fluid film tube formed on the solid (nonsuperfluid) layers about 0.5 nm in thickness has the diameter of about 1.8 nm in the 2.8 nm pore (as illustrated at upper right corner in Fig. 9) whose length is about 300 nm, the same as the grain size of the FSM substrate. We assume continuous phonon dispersion relation for wave vector along the tube with the velocity v_C and discrete energy states for the motion along the circumference of the nanotube with the gap Δ between the ground state and the first excited state. The calculated heat capacity becomes the 1D phonon heat capacity below $1/10$ of Δ/k_B and crossovers from the T- to T^2-dependence due to the thermal excitation to excited states in the cross section [39]. Fitting the calculation to the data, the coverage dependence of v_C and Δ/k_B were obtained as shown in Fig. 9(b) [39]. The phonon velocity v_P in the fluid layers is alternatively estimated from the pressure isotherms (Fig. 3(b)) in the same procedure as that for Hectorite (Sect. 4.2). v_P of the fluid layers above 20 μmol/m^2 are also shown in Fig. 9(b) [40]. Both velocities of v_C and v_P agree within the uncertainties. In the case of the 2.7 nm 3D nanopores (HMM-2), the low temperature heat capacities (Fig. 10(a)) are fitted by the 3D phonon model ($C \propto T^3$) [40]. The phonon velocity v_C is plotted in Fig. 10(b), together with v_P estimated from the pressure isotherms.

Since the low-temperature heat capacities in the (B)-phases are well described by the thermal phonon excitations, the 1D and 3D states are defined by the thermal phonon wavelength. The 1D state is defined as being when the thermal phonon

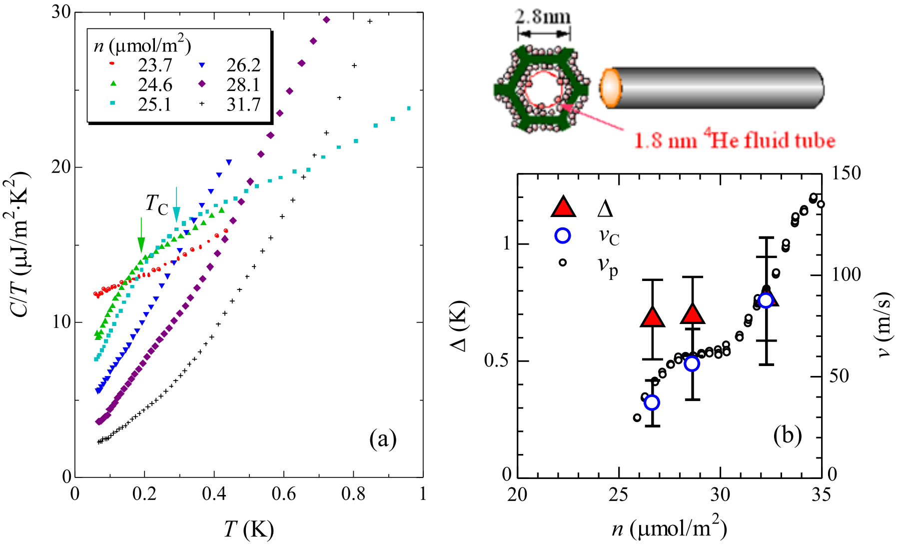

Fig. 9 (Color online) (**a**) C/T of ^{4}He in 1D (2.8 nm) nanopores of FSM at $n \geq 1.4n_1$ where fluid film is formed on a nonsuperfluid layer. Rounded cusp at T_C suggests the onset to the (B)-phase of the ^{4}He fluid tube 1.8 nm in diameter formed in the 2.8 nm-diameter pore (illustrated at *upper right corner*). (**b**) Phonon velocity v_C and gap energy Δ in the cross section of the fluid nanotube estimated from the heat capacity. Phonon velocity v_P estimated from vapor pressure for adsorption (see the text)

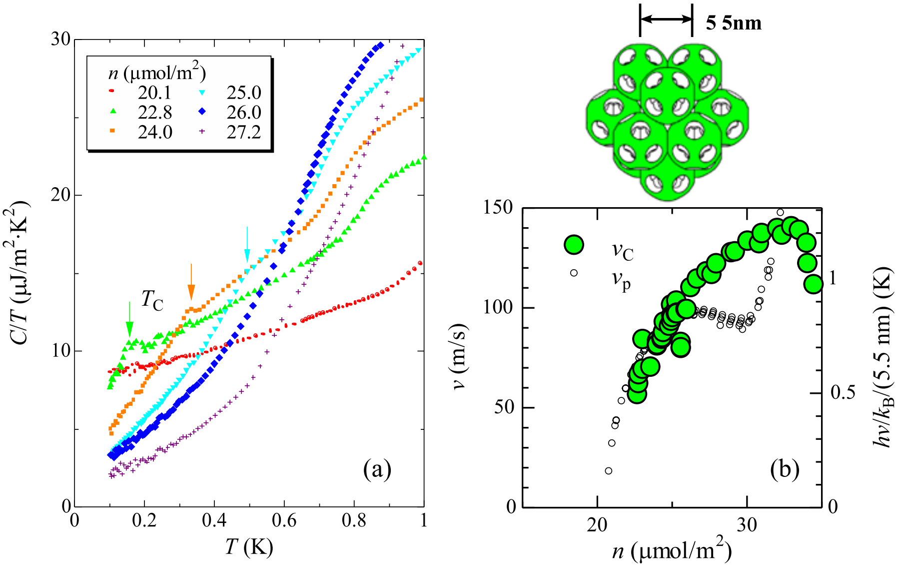

Fig. 10 (Color online) (**a**) C/T of ^{4}He in 3D (2.7 nm) nanopores of HMM-2 at $n \geq 1.4n_1$ where fluid film is formed on an nonsuperfluid layer. The film is connected by 5.5 nm in the 3D period. (**b**) 3D phonon velocities v_C and v_P estimated from heat capacity and pressure isotherm, respectively. hv/k_B (5.5 nm) is the temperature where the thermal phonon wavelength is equal to the 3D period (see the text)

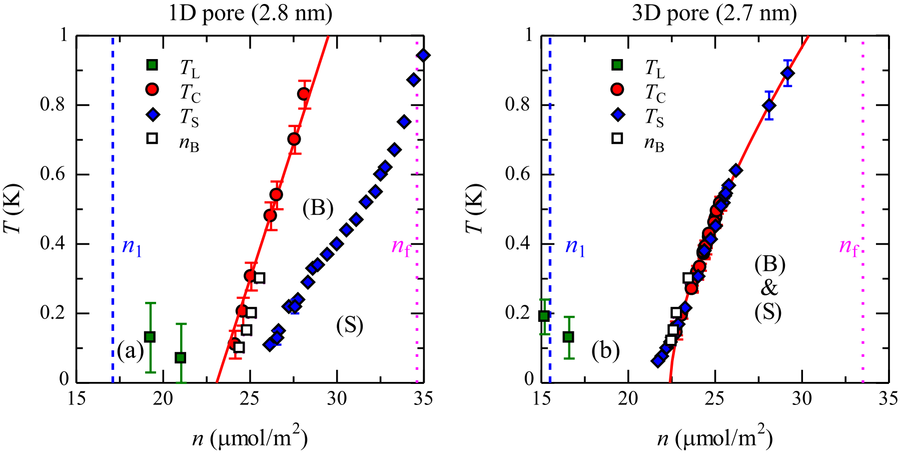

Fig. 11 (Color online) (**a**) Phase diagram of ^{4}He in 1D (2.8 nm) pore of FSM. T_C, (B) phase boundary, linearly increases with n (*solid line*). Superfluid onset temperature T_S is far below T_C. (**b**) Phase diagram of ^{4}He in 3D (2.7 nm) pore. $T_S = T_C$, and the superfluid transition temperature changes as $(n - n_{c'})^{2/3}$ (*solid curve*) (see the text)

length $h v_C / k_B T$ becomes longer than the fluid tube diameter which is 1.8 nm by subtracting the nonsuperfluid layer thickness 0.5 nm from the pore diameter 2.8 nm. The 1D phonon state calculated from v_C given in Fig. 9(b) is below about 0.8 K in the (B)-phase (Fig. 11(b)). This temperature 0.8 K is almost equal to the gap temperature Δ / k_B in the cross section (Fig. 9(b)). In the case of the 3D pores, the 3D state is defined as being when the thermal phonon wavelength exceeds the 3D period of 5.5 nm, or $T \le h v_C / k_B /(5.5\ \mathrm{nm})$ (Fig. 10(b)). Thus, in terms of the thermal phonon excitations, the (B)-phases below about 1 K are 1D and 3D, respectively [8].

5 Superfluidity of ^{4}He Films Formed in 1D and 3D Nanopores

5.1 Superfluid Onset and Transition in 1D and 3D Nanopores

Superfluidity is the most interesting issue for the ^{4}He fluids in the 1D and 3D nanopores, as well as for the bulk ^{4}He liquid and the 2D KT transition. To our knowledge, there is no common understanding of the superfluidity in the 1D state. For the ^{4}He films adsorbed in the macropores of Vycor glasses, Reppy et al. observed evidence of the 3D superfluid transition [10] and proposed the possible BEC of the 3D ideal gas due to the 3D pore connection [7]. On the other hand, the Bose glass transition model was alternatively proposed, assuming that the random potential of the substrate plays the most important role [12].

FSM (1D (2.8 nm) pore) and HMM-2 (3D (2.7 nm) pore) have the same pore diameter and substrate potentials (Sect. 3.3). To study the dependence of the superfluidity on the dimensionality of the pore connection, we measured simultaneously the heat capacity and the superfluid density by a torsional oscillator at exactly the same ^{4}He coverage [8]. Figure 12(a) shows C/T and the oscillator frequency shift

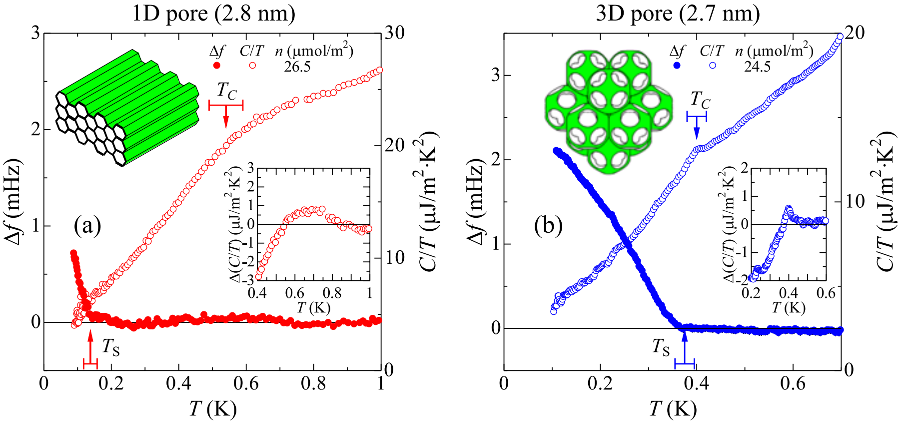

Fig. 12 (Color online) Simultaneous measurements of superfluid density ($\propto \Delta f$) and heat capacity (C) of ^{4}He adatoms. (**a**) In 1D (2.8 nm) pore, superfluid onset temperature T_S is far below the rounded cusp at T_C of the heat capacity C. (**b**) In 3D (2.7 nm) pore, T_S coincides with peak temperature T_C of the heat capacity

Δf due to the superfluid at the same coverage $n = 26.5$ μmol/m^2 adsorbed in the 1D (2.8 nm) pores. C/T shows a rounded cusp at $T_C = 0.5$ K. The rounded anomaly is magnified in the inset where $\Delta(C/T)$ is the difference of C/T from a linear extrapolation from high temperatures above T_C. The superfluid onset occurs at $T_S = 0.13$ K, far below T_C. In the phase diagram (Fig. 11(a)), the superfluid observed region (S) determined by T_S is a low temperature region of the (B)-phase. In contrast, for the 3D (2.7 nm) pores, C/T at $n = 24.5$ μmol/m^2 exhibits a sharp kink at $T_C = 0.39$ K with a small but a sharp peak, as shown in Fig. 12(b). Furthermore, the superfluid onset appears at the same temperature ($T_S = T_C$), within the experimental uncertainty. Thus, the (S)-region completely overlaps the (B)-phase (Fig. 11(b)).

The superfluid density ($\propto \Delta f$) and the amplitude observed by the torsional oscillator are shown in Figs. 13(a) and (b). In case of 1D (2.8 nm) pores, Δf increases rather rapidly just below the onset temperature T_S, together with a dissipation peak (a minimum of the amplitude). The dissipation is observed to the lowest temperature measured. These are rather similar to those of the KT transition [2]. While, in the case of 3D (2.7 nm) pores, Δf increases in a power law below T_S. We observed no dissipation except for the small peaks (dips of amplitude) due to the coupling with the third sound standing waves. These properties of the 3D ^{4}He films indicate the 3D long range order transition.

Thus, the ^{4}He fluid films formed in the nanopores clearly show the dependence of the superfluidity on the 1D and 3D pore connections.

5.2 Comparison with 1D to 3D Ideal Bose Gases

In the book by F. London [41], he addressed various properties of the bulk liquid ^{4}He, and proposed the relation between the superfluid and the BEC of the ideal 3D Bose gas. Although there are large interactions in the ^{4}He liquid, the superfluid transition

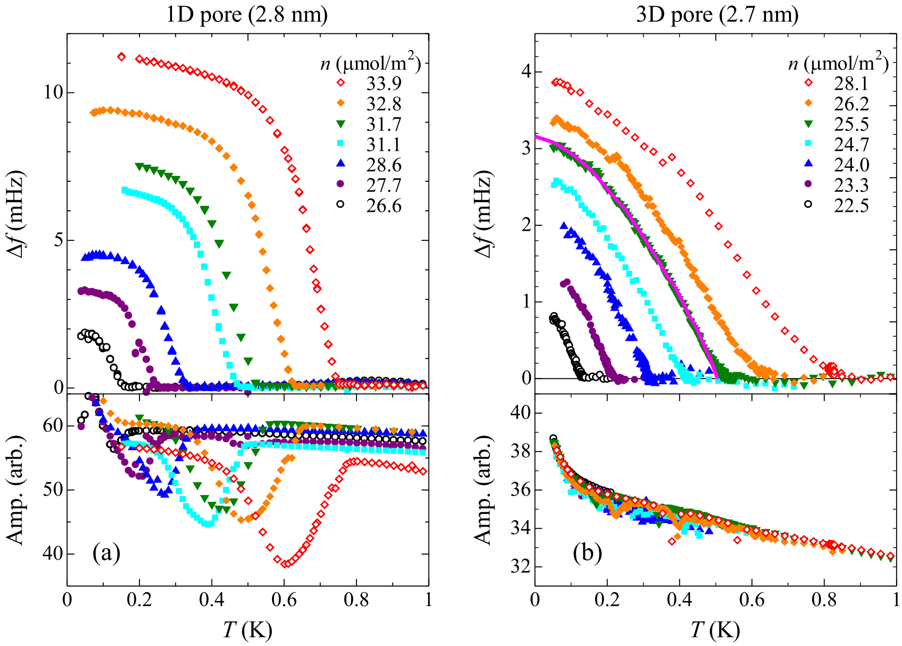

Fig. 13 (Color online) (**a**) Δf of superfluid density and amplitude of torsional oscillator for 1D (2.8 nm) pore. Below the superfluid onset, a steep increase of Δf and a dissipation (decrease of amplitude) are observed. (**b**) Δf and amplitude for 3D (2.7 nm) pore. *Solid curve* is the superfluid density calculated for a 3D atomic gas. Dissipation due to superfluid onset is not observed, except for dips of amplitude by resonances with the third sound

Fig. 14 (Color online) Specific heats (C/nR) of 1D, 2D and 3D ideal Bose gases. Temperature (T) is normalized by T_0 where the thermal de Broglie wavelength λ_T is equal to the mean particle distance. T_{3D-BEC} is the BEC temperature of the 3D gas. T^*_{2D} is the crossover temperature from the almost constant Boltzmann specific heat to the T-linear dependence

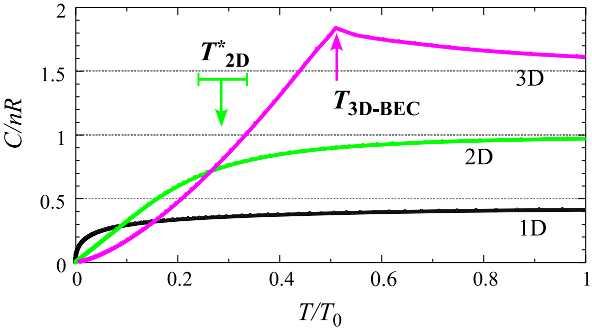

temperature 2.2 K of the bulk ^{4}He liquid is the same order as the BEC temperature T_{3D-BEC} =3.2 K, calculated for the non-interacting gas at the same density. Here, we compare the (B)-phases and the superfluids observed in the 1D and 3D nanopores with the Bose gases in one-, two- and three-dimensions [8, 42].

Figure 14 shows specific heats C/n of ideal Bose gases from 1D to 3D, where T is normalized for T_0 at which the thermal de Broglie wavelength $\lambda_T = h/\sqrt{2\pi m k_B T_0}$ is equal to the mean particle distance calculated from the number density. It is well known that the 1D and 2D Bose gases do not set into BEC at finite temperatures. However, both C/n show the crossovers from almost constants at high temperatures to the power law decreases at low temperatures. In the case of the 2D Bose gas (Fig. 14), the crossover occurs at $T^*_{2\mathrm{D}}/T_0 = 0.28 \pm 0.05$ that is an intersection of the extrapolated Boltzmann region ($C/nR \sim 1$) with the extrapolated degenerate region. The crossover temperature $T^*_{2\mathrm{D}}$ is proportional to the 2D density $n_{2\mathrm{D}}$ in the rate $(0.13 \pm 0.02)\ \mathrm{K}/(\mu\mathrm{mol/m}^2)$. In the 3D Bose gas (Fig. 14), BEC occurs at $T_{3\mathrm{D-BEC}}/T_0 = 0.51$, accompanying a peak of C/nR. The BEC temperature is described as $T_{3\mathrm{D-BEC}} = \frac{2\pi\hbar^2}{k_{\mathrm{B}}m}(\frac{N_{\mathrm{A}}n_{3\mathrm{D}}}{2.612})^{2/3}$, where m is an atomic mass, N_{A} is Avogadro's number and $n_{3\mathrm{D}}$ is the 3D gas density. $T_{3\mathrm{D-BEC}}$ increases in the 2/3-power law of the density.

In the case of the 1D nanopores, T_C, where C/T shows the rounded cusp (Figs. 9(a) and 12(a)), is proportional to the density n as shown in Fig. 11(a). This relation can be compared with the linear dependence of $T^*_{2\mathrm{D}}$ (Fig. 14) of the 2D Bose gas on $n_{2\mathrm{D}}$. The fluid film in the 1D pores can be regarded as a 2D free particle gas at T_C, because λ_T is shorter than the circumference of the 1.8 nm fluid tube. T_C in Fig. 11(a) changes at the rate 0.18 K/(μmol/m^2). Since the 1D diameter reduces from the 2.8 nm to 1.8 nm for the fluid tube by the solid (nonsuperfluid) layer 0.5 nm in thickness, the rate should be corrected to 0.12 K/(μmol/m^2), in order to compare with $T^*_{2\mathrm{D}}/n_{2\mathrm{D}} = (0.13 \pm 0.02)\ \ \mathrm{K}/(\mu\mathrm{mol/m}^2)$ of the 2D ideal gas (Fig. 14). This rate agrees within the uncertainty in the adsorption area [42].

In the 1D nanopores (Figs. 11(a) and 12(a)), an anomaly of the heat capacity is observed at T_C and the superfluid onset at T_{S} far below T_C. In the Ginzburg-Landau theory, the order parameter appears at a temperature T_{GL} accompanying a peak (anomaly) of the heat capacity. T_C is likely to correspond to T_{GL}. The 2D KT transition occurs far below T_{GL} without heat capacity anomaly. This is similar to the superfluid onset at T_S. Rather steep increase of the observed superfluid density just below T_{S} (Figs. 13(a)) is similar to the universal jump at T_{KT}. The observed superfluid density is equal to the stiffness of the phase coherence. Yamashita and Hirashima [43] calculated the anisotropic stiffness of the film tubes in the 1D pores with the asymmetry ratio of the tube length divided by the circumference. In addition to the aspect of the vortex pairing and unbinding in the usual KT theory [3], the 1D thermal fluctuations of the long wavelength (phonon) along the tube reduce the stiffness (the observed superfluid density) with increasing temperature. A large reduction of the stiffness also occurs above a ratio of the asymmetry.

In the present 3D nanopores, 5.5 nm in regular 3D period, the heat capacity has a small but obviously sharp peak at T_C (Fig. 12(b)), in contrast to the rounded peak in the 1D pores (Fig. 12(a)). Furthermore, the 3D transition is clearly indicated by the superfluid onset occurring at the heat capacity peak temperature ($T_{\mathrm{S}} = T_C$) [8]. The coverage n dependence of T_C (Fig. 11(b)) is well fitted with $T_{3\mathrm{D-BEC}}$ of the ideal 3D Bose gas, as shown by the solid curve. Here, we assume the bare ^{4}He atomic mass m and the 3D gas density $n_{3\mathrm{D}}[\mu\mathrm{mol/m}^3] = 8.26 \times 10^8\ [\mathrm{m}^{-1}]\ (n - n_{\mathrm{c}'})[\mu\mathrm{mol/m}^2]$, where the fluid $(n - n_{\mathrm{c}'})$ on the nonsuperfluid layer of $n_{\mathrm{c}'} = 22.4\ \mu\mathrm{mol/m}^2$ is homogeneously averaged within the total volume of the substrate frame and the void. The calculated $T_{3\mathrm{D-BEC}}$ well reproduces the 2/3-power law of the (B)-phase ((S)-phase) boundary above about 0.15 K. The deviation near the onset coverage $n_{\mathrm{c}} \approx 21\ \mu\mathrm{mol/m}^2$ may

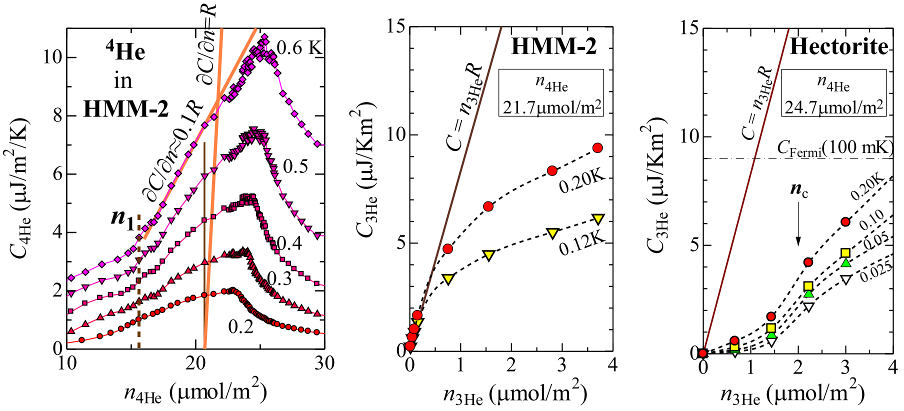

(a) (b) (c)

Fig. 15 (Color online) (**a**) C-isotherms of ^{4}He adsorbed in 3D (2.7 nm) pore of HMM-2. Above n_1, specific heat of the second layer in the normal fluid state is the order of $0.1R$ which is much smaller than R or $1.5R$ of the Boltzmann gas. (**b**) C-isotherms of ^{3}He adsorbed in HMM-2 preplated with ^{4}He (21.7 μmol/m^2). $\partial C/\partial n \approx R$ at low coverages indicates the non-interacting Boltzmann gas state of the ^{3}He adatoms. (**c**) C isotherms of ^{3}He adsorbed in Hectorite (OH02) preplated with ^{4}He (24.7 μmol/m^2). Small heat capacity below $n_{\text{c}} \approx 2$ μmol/m^2 suggests the localization of ^{3}He adatoms

be due to the increase of the nonsuperfluid layer coverage from n_{c} to $n_{\text{c}'}$ by the promotion of the fluid layers or perhaps due to the Bose glass transition.

The observed superfluid density of the ^{4}He films in the 3D pores does not show the universal jump characteristic of the usual KT transition. Instead, its temperature dependence below T_{S} ($= T_C$) is well reproduced by the calculation for the BEC of a 3D atomic gas as marked with the solid curve [44] in Fig. 13(b), where the calculated curve is normalized to T_{S} and the superfluid density at 0 K.

Thus, the observed heat capacities and superfluidity of ^{4}He in the 1D and 3D nanopores have the similarities to those of the Bose gases in various dimensions. The ^{4}He fluid film tubes formed in the 1D (2.8 nm) pores show the 2D and 1D properties depending on the temperature [39]. The superfluid onset of the ^{4}He nanotubes is possibly understood by the anisotropic model of the KT transition [43]. The ^{4}He nanotubes are in the 1D state at the sufficiently low temperatures where the thermal phonon wavelength is longer than the pore diameter [45]. In the 3D pores, the ^{4}He fluid films obviously show the 3D superfluid transition and similarities of $T_C - n$ and $\rho_{\text{S}} - T$ to those of the 3D atomic gas [8].

6 ^{3}He Fluids Formed in 1D and 3D Nanopores

6.1 Realization of ^{3}He Gases at Low Densities

In contrast to the ground state at $k = 0$ of the Bose gases, the degenerate state of a ^{3}He fluid has the Fermi energy E_{F} and the wave number vector k_{F} ($= \sqrt{2m^* E_{\text{F}}}/\hbar$), both of which increase with the density n. As explained in Sect. 6.2, an actual 1D

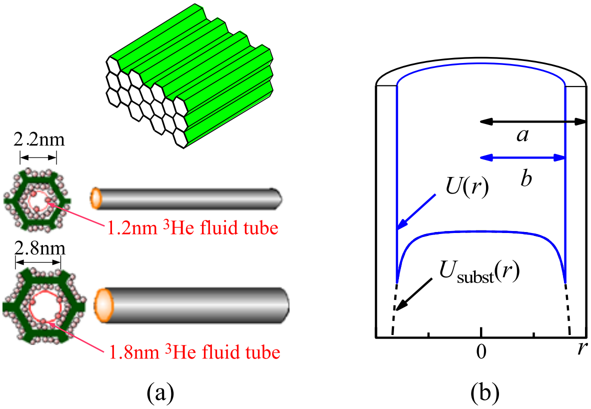

Fig. 16 (Color online) (**a**) ^{3}He fluid nanotubes 1.2 and 1.8 nm in diameter formed in 1D 2.2 and 2.8 nm pores preplated with ^{4}He, respectively. (**b**) Model of potential for a ^{3}He atom. Substrate potential $U_{\mathrm{subst}}(r)$ in a pore $2a$ in diameter has the dependence of $(a-r)^{-3}$ near the pore wall and a maximum at the center ($r=0$) of the pore. In the pores preplated with ^{4}He $(a-b)$ in thickness, effective potential $U(r)$ for a ^{3}He atom has the potential wall at $r=b$

Fermi fluid of ^{3}He in 1D nanopores is realized at sufficiently low densities where the Fermi wavelength $2\pi/k_{\mathrm{F}}$ becomes longer than the pore diameter, as well as at lower temperatures than T_{F}. So, we must recognize the gas state of the adsorbed ^{3}He at sufficiently low fluid densities.

When thin fluid layers are promoted on the solid (inert) ^{3}He layers above 1–$1.4n_1$ in Figs. 7(a) and (b), $\partial C/\partial n$ of the ^{3}He isotherms are much smaller than the gas constant R in the normal fluid state. The small specific heat $\partial C/\partial n$ is also observed for ^{4}He adsorbed in HMM-2, as shown in Fig. 15(a) [46, 47]. In the normal fluid state between 21.7 μmol/m^2 (superfluid onset coverage at 0 K) and the peak coverage n_{B} (superfluid and (B)-phase boundary), $\partial C/\partial n$ is the order of $0.1R$. Figure 15(b) shows the isotherms of ^{3}He when small amounts of ^{3}He were adsorbed on the pore walls preplated with ^{4}He of $n_{^4\mathrm{He}} = 21.7$ μmol/m^2. At the sufficiently low densities of ^{3}He, the specific heats are the order of R, which clearly indicates the Boltzmann gas state of the ^{3}He adatoms. These completely different specific heats of the thin ^{3}He fluid films formed on ^{4}He and pure ^{3}He layers suggest that a quantum atomic exchange interaction between the fluid and the solid (inert) layers which occurs in the case of the same isotope helium atoms [6].

In the case of Hectorite preplated with 24.7 μmol/m^2 of ^{4}He (Fig 15(c)), the specific heat of ^{3}He is small below $n_{\mathrm{c}} \approx 2$ μmol/m^2. This indicates the localization of the ^{3}He adatoms at the low coverages. Since there are Na$^+$ localization potentials on the substrate of Hectorite (Fig. 2), ^{3}He atoms on the ^{4}He layers are likely to be localized near Na$^+$ cations, similar to the electrons in Si:P [47].

In FSM as well as HMM-2 whose pore walls are made of silicates, the ^{3}He atoms adsorbed on the ^{4}He layers are likely to be a noninteracting gas with the specific heat of the order of R [46]. Next, we consider the dimensionality of the ^{3}He gases with 1D and 3D pore connections with nano-diameters.

6.2 1D ^{3}He Gas Formed in 1D Nanopores

The 1D nanoporous material FSM are powder whose grain sizes are about 300 nm. Each grain has a honeycomb structure which has 1D channels on the order of 300 nm in length (Fig. 16(a)). The 1D nanopore walls of FSM with the pore diameters $2a =$

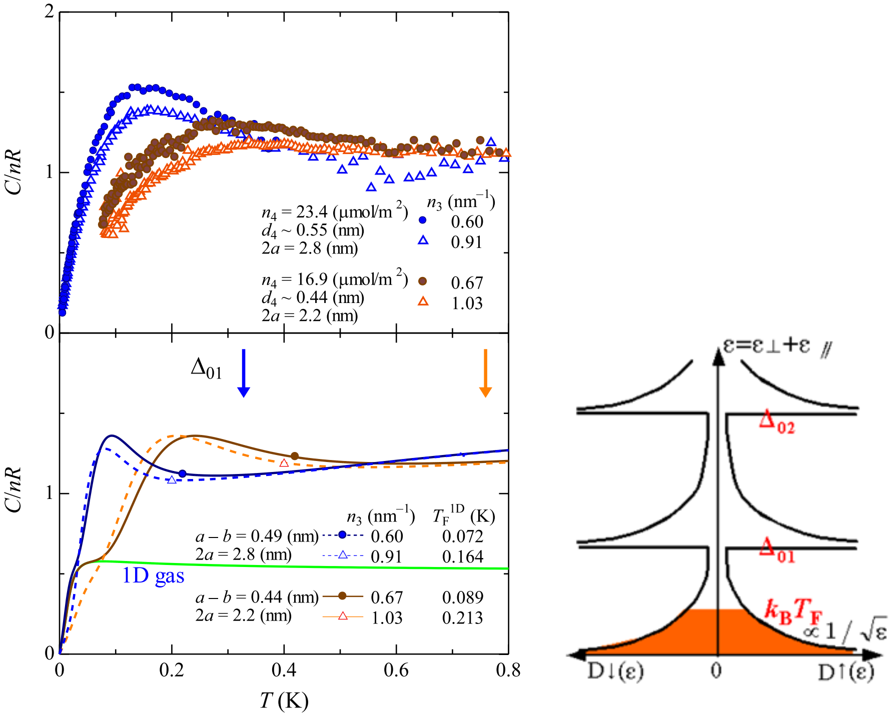

(a) (b)

Fig. 17 (Color online) (**a**) Heat capacities C of ^{3}He nanotubes formed in 1D (2.8 and 2.2 nm) pores preplated with ^{4}He of $n_{^4\mathrm{He}}$, experiment (*upper*) and calculation (*lower*). (**b**) Schematic density of states $D(\varepsilon)$ of a ^{3}He gaseous nanotube

2.8 and 2.2 nm are preplated with ^{4}He at 23.4 and 16.9 μmol/m^2, respectively, and adsorbed ^{3}He. Considering the thickness of the ^{4}He layers, nanotubes of ^{3}He about 1.8 and 1.2 nm in diameter are formed in the 1D nanopores, as shown in Fig. 16(a).

The upper panel in Fig. 17(a) shows the heat capacities measured at the lowest two ^{3}He coverages n_3 in the unit of number of atoms per unit tube length of the 2.8 and 2.2 nm pores, respectively. For all coverages, C/n_3R approaches unity at high temperatures above 0.4(0.6) K in 2.8(2.2) nm pores. This strongly suggests that the film behaves as a 2D Boltzmann gas. As the temperature is decreased, C/n_3R at the lowest coverage increases and shows a maximum around 0.14(0.28) K. At the lower temperatures, C/n_3R approaches linear in T, which indicates the degenerate state of the ^{3}He nanotubes.

Here, we calculate the heat capacity of the ^{3}He nanotubes in the 1D nanopores. In the nanopore with a cylindrical geometry, the potential $U_{\mathrm{subst}}(r)$ from the substrate is calculated as shown in Fig. 16(b), using proper potential parameters and a method [48]. When the nanopore $2a$ in diameter is preplated with ^{4}He, the potential $U(r)$ for a ^{3}He atom can be described by having a potential wall at $r = b$, where the preplated ^{4}He layer has $(a - b)$ in thickness. The eigenstate of the Schrödinger equation for the motion in the potential $U(r)$ is described by the number of nodes, ℓ and m, of the eigenfunction for the radius and the azimuthal angle, respectively. The ground state with $\ell = 0$ and $m = 0$ and the first excited doublet with $\ell = 0$ and $m = 1$ are the 2D states ($\ell = 0$) having a probability peak near the wall. We describe the gap energy between them as Δ_{01}. Δ_{01}/k_B was calculated to be 0.33(0.76) K for 2.8(2.2) nm 1D pores preplated with ^{4}He, as indicated by arrows in the lower panel of Fig. 17(a). The 3D excited states with $\ell \neq 0$ have energies much higher than Δ_{01}. The motion along the tube is the free translation with the 1D density of state ($\propto 1/\sqrt{\varepsilon_\|}$). Thus, the total density of state $D(\varepsilon)$ is described as shown schematically in Fig. 17(b). At a low coverage n_3, the Fermi energy $k_B T_F$ is much lower than Δ_{01}. The lower panel in Fig. 17(a) is the heat capacities calculated in the conditions corresponding to the experiments. At the lowest n_3, C/n_3R approaches unity above about the gap temperature Δ_{01}/k_B. A little larger C/n_3R than unity is due to the thermal excitations to the 3D states with $\ell \neq 0$. With decreasing T, the heat capacity shows the Schottky peak at 1/3 of Δ_{01}/k_B, and approaches linear in T. Below 1/10 of Δ_{01}/k_B, C/n_3R literally agrees with that of the 1D Fermi gas. The dimensional crossover from 2D to 1D with decreasing T is indicated by the Schottky peak at 1/3 of Δ_{01}/k_B. The peak becomes small with increasing coverage, and disappears when the Fermi energy becomes larger than Δ_{01}.

The calculated temperature dependences semiquantitatively reproduce the experimental results, as shown in Fig. 17(a). The pore size dependence of the dimensional crossover is also well reproduced by the calculation. Thus, the 1D Fermi gases are realized for the ^{3}He fluid nanotubes formed in the 1D pores at sufficiently low coverages as well as the low temperatures.

6.3 Degenerate States of ^{3}He Nanotubes

To study the degenerate state of the ^{3}He nanotubes about 1.8 nm in diameter formed in the 2.8 nm 1D nanopores preplated with ^{4}He, heat capacity C was measured at low temperatures, as shown in Fig. 18(a) [27]. The degenerated state is clearly indicated by approaching the linear-in-T dependence with decreasing temperature. The data are fitted to the equation, $C = \beta_0 + \gamma T + \beta_2 T^2$. Dependences of the obtained parameters on coverage n are shown in Fig. 18(b)–(d). The γT-term corresponds to that of the Fermi degeneracy.

In the case of D ($= 1, 2$ or 3)-dimensional non-interacting Fermi gas, the density n dependence of the γ-value is described as $\gamma \propto n^{1-2/D}$. The observed γ-value increases monotonically with increasing n_3 (Fig. 18(c)). The dependence is explained by neither 1D nor 2D ideal Fermi gas. One possible model is to assume an inhomogeneity of the 1D pore diameters so that the density of the states increases with the density [49]. Another model is to assume a puddling due to a binding energy between ^{3}He atoms: an apparent γ is proportional to the amount of the puddling, i.e. n. The binding energy between the two helium atoms has been studied in various dimensions and pores [6, 50, 51]. In the 3D free space, the bound state energy for ^{4}He atoms was observed to be a few mK. On flat substrates, a bound state or a puddling of ^{3}He has not been observed in many conditions, except for low ^{3}He densities adsorbed on the ^{4}He layers of 1.0- and 1.23-nm thickness formed on a Nuclepore filters [52, 53]. In the 1D Fermi gas, the Fermi energy increases quadratic to the density, while

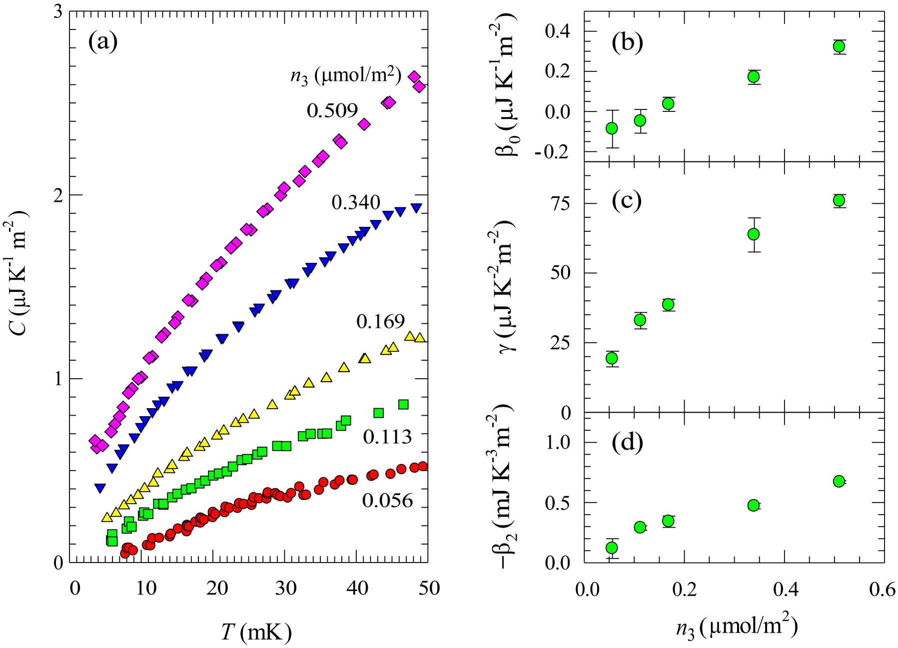

Fig. 18 (Color online) (**a**) Low temperature heat capacities of degenerate ^{3}He in 1D (2.8 nm) pores preplated with ^{4}He. Data are fitted to $C = \beta_0 + \gamma T + \beta_2 T^2$. (**b**–**d**) Coverage n_3 dependences of β_0, γ and $-\beta_2$, respectively

the two-body interaction increases in proportion to the density. Hence, these dependences indicate a bound state if there is minimal attractive interaction. Furthermore, the magnitude of the bound state energy strongly depends on pore size and potential in the pores, e.g., 25 mK in a cylindrical pore 1.4 nm in diameter [50], and about 1 K in a carbon nanotube [54]. To solve the bound state or puddling, an actual potential and geometry in the present 1D pores should be taken into account.

6.4 ^{3}He Gas in 3D Nanopores

In the 3D nanopores of HMM-2 preplated with ^{4}He (n_4), nearly free ^{3}He Boltzmann gas was indicated by the specific heat as large as R, as shown in Fig. 15(b). The ^{3}He fluid films are topologically connected in 3D with the period 5.5 nm through the pores about 2.7 nm in diameter. The flat pore wall size in the 3D nanopores is estimated to be about 2.8 nm (= (5.5−2.7) nm).

Temperature dependence of the ^{3}He heat capacity is shown for various ^{3}He coverages n_3 in Fig. 19, which also indicates the thermal de Broglie wavelength λ_T and n_3 together with the mean distance $\bar{r}$ and the Fermi temperatures $T_{2\mathrm{DF}}$ and $T_{3\mathrm{DF}}$ estimated for 2D and 3D, respectively [55]. The ^{3}He fluid at the lowest coverage n_3 is in the Boltzmann gas state down to the lowest temperature measured, because both $T_{2\mathrm{DF}}$ and $T_{3\mathrm{DF}}$ are sufficiently low. Above about 0.4 K, $C_3/n_3R \approx 1$ (at the low coverages with $T_{2\mathrm{DF}} \ll 0.4$ K) is the heat capacity of the 2D Boltzmann gas, where λ_T

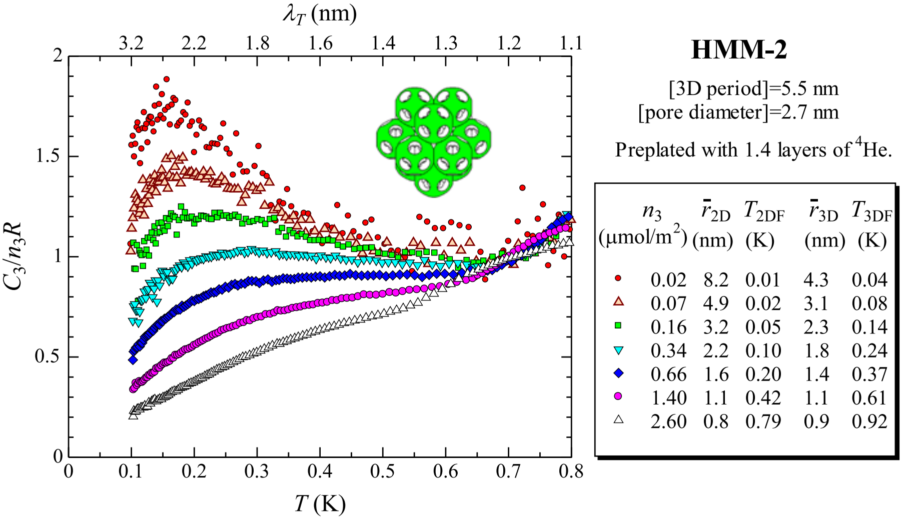

	n_3 (μmol/m^2)	$\bar{r}_{2D}$ (nm)	T_{2DF} (K)	$\bar{r}_{3D}$ (nm)	T_{3DF} (K)
●	0.02	8.2	0.01	4.3	0.04
△	0.07	4.9	0.02	3.1	0.08
■	0.16	3.2	0.05	2.3	0.14
▽	0.34	2.2	0.10	1.8	0.24
◆	0.66	1.6	0.20	1.4	0.37
●	1.40	1.1	0.42	1.1	0.61
△	2.60	0.8	0.79	0.9	0.92

Fig. 19 (Color online) Heat capacities of ^{3}He adsorbed in 3D (2.7 nm) pores of HMM-2 preplated with ^{4}He at $n_{4\mathrm{He}} = 21.7$ μmol/m^2. λ_T is the thermal de Broglie wavelength of a ^{3}He atom. $\bar{r}$ is the mean interparticle distance, and T_F the Fermi temperatures for 2D and 3D at each ^{3}He coverage n_3

(< 1.6 nm) is much smaller than the pore wall size (≈ 2.8 nm). At the lower temperatures, the heat capacity becomes comparable to $C_3/n_3R = 1.5$ of the 3D Boltzmann gas. λ_T becomes longer than the 3D period (5.5 nm) below 34 mK, where the ^{3}He fluid films result in the 3D gas. The heat capacity in the 3D-2D crossover has not been calculated. Furthermore, the degenerate states of the new 3D ^{3}He fluids should be studied experimentally and theoretically.

7 Other Topics of Helium Adatoms

7.1 Microscopic Properties of Superfluid Vortices in ^{4}He Films

Under the nano-extreme conditions of the 1D and 3D nanopores, the superfluid onsets (transitions) of the ^{4}He films have obviously different properties depending on the film (pore) connections (Sect. 4.3). The ^{4}He fluid films formed on flat solid surfaces are known to be the 2D Kosterlitz-Thouless superfluid transition where the superfluid vortices play the major role [3]. Although the most important vortex parameters (the diffusion constant D, the core diameter a_0) have been experimentally obtained [56–61], these have not sufficient accuracies in various conditions even for the typical 2D KT transition. Here, the microscopic vortex parameters are precisely estimated by the dependence of the superfluid onset on the extremely high measurement frequency at the temperatures between 0.05 and 0.9 K [62].

In the usual superfluid measurement by a torsional oscillator at about 1 kHz, the observed superfluid density shows the universal jump at the KT transition temperature T_KT [2]. We measured the superfluid density by a quartz-crystal-microbalance

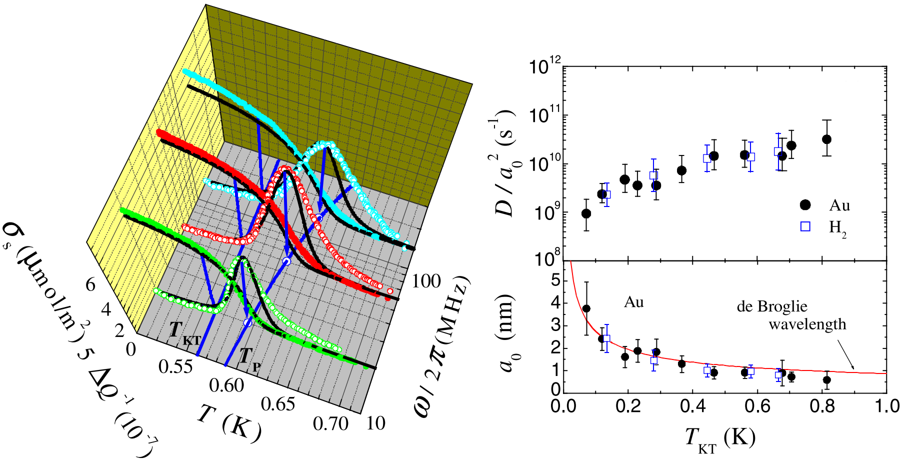

(a) (b)

Fig. 20 (Color online) (**a**) Frequency dependences of superfluid density σ_s and dissipation ΔQ^{-1} at the same coverage, 37.7 μmol/m^2. Onset temperature and dissipation peak temperature T_p increase with increasing frequency. *Solid curves* are calculations using $T_{KT} = 0.561$ K, $D/a_0{}^2 = 1.9 \times 10^{10}$ sec^{-1}, and $b = 7$ for the frequencies 20, 60 and 140 MHz, respectively. (**b**) (*upper*): Vortex parameter $D/a_0{}^2$ vs. T_{KT} for the gold (*solid circles*) and H_2 preplated (*open square*) gold, respectively. (*Bottom*): Vortex core diameter a_0 estimated by assuming the quantum diffusion limit $D = \hbar/m$ (*solid circles and open squares*). *Solid curve* is the thermal de Broglie wavelength at T_{KT}

(QCM) at 20–180 MHz [62], 10^{4-5} times higher than 1 kHz of the torsional oscillator. Figure 20(a) shows the observed superfluid densities at 20, 60, and 140 MHz, respectively, for exactly the same coverage $n = 37.7$ μmol/m^2 of the ^{4}He on gold. The superfluid onset temperature and the dissipation peak temperature T_p are obviously higher than T_{KT}, and they increase with increasing frequency $\omega/2\pi$. At 140 MHz, the onset temperature at 0.7 K is about 25% higher than $T_{KT} = 0.561$ K.

These large frequency dependences are well reproduced by the recursion calculation in the dynamic KT theory [63]. The dissipation peak temperature T_p is calculated as $\frac{T_p - T_{KT}}{T_{KT}} = \frac{4\pi^2}{b^2}(\frac{1}{2}\ln\frac{14D}{a_0{}^2\omega})^{-2}$, where b is a constant. Note that this equation is correct in the angular frequency ω lower than $14D/a_0{}^2$. From the fitting, D/a_0^2 on the gold substrate was accurately obtained as shown in Fig. 20(b), where T_{KT} is proportional to the coverage. When the substrate is preplated with H_2, the superfluid onset coverage becomes about 1/3, indicating a large change of the adsorption potential by the preplating, but D/a_0^2 has the same value as shown in Fig. 20(b) [64]. This suggests that the diffusion constant D on both substrates is the largest value $\hbar/m$ at the quantum diffusion limit. Then the core diameter a_0 is estimated to be the same magnitude as the de Broglie wavelength at T_{KT}, as shown in Fig. 20(c).

Thus, the study at extremely high frequencies precisely determines the microscopic properties of the superfluid vortices of the ^{4}He fluid films. Substrate dependence of the vortex parameters is likely to be observed [62]. It will allow to study at the breakdown frequency condition for the present dynamic theory where the fre-

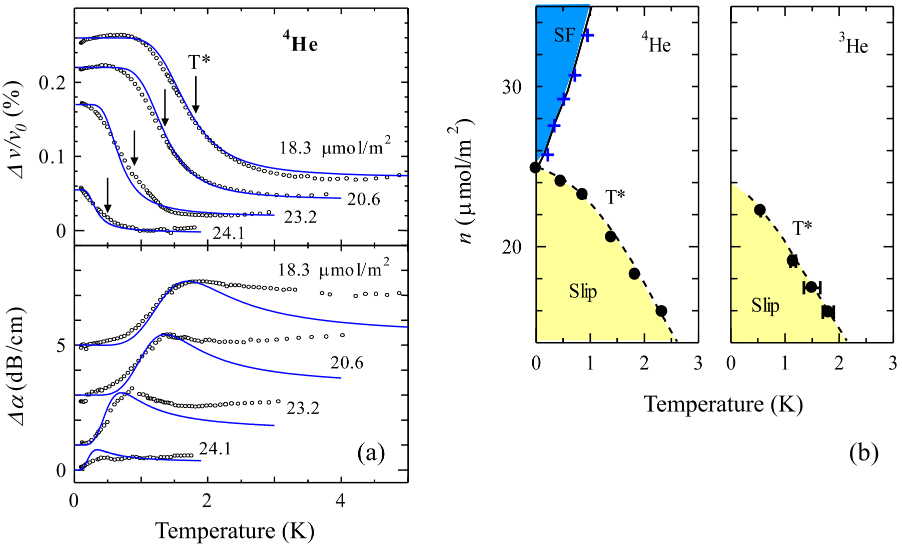

Fig. 21 (Color online) (**a**) Sound velocity change $\Delta v/v_0$ and excess attenuation $\Delta\alpha$ due to slippage of nonsuperfluid ^{4}He films at 10 MHz. (**b**) Phase diagrams for ^{4}He and ^{3}He films. Slip: slippage region below T^*, and SF: ^{4}He superfluid observed by ultrasound and torsional oscillator

quency $\omega/2\pi$ becomes larger than $(14/2\pi)D/a_0^2$ by changing these vortex parameters.

7.2 Slippage of Helium Adatoms in Non-superfluid State

Usually, the fluidity is a distinct property of the gas and the liquid states individualized from the solid state. However, a superflow in the solid ^{4}He was observed by a torsional oscillator experiment [65]. In the study using the quartz-crystal-microbalance (QCM) at the frequency $\approx 10^7$ Hz, Krim and her colleagues [66, 67] observed a slippage of the Kr atoms physisorbed on a gold substrate against the shear vibration of the substrate at 77 K. Hieda and Suzuki investigated the dynamic response (fluidity or slippage) of the helium atoms adsorbed in Hectorite by the ultrasound measurement.

The ultrasound technique was first used to observe superfluidity of the ^{4}He films adsorbed in Vycor glass [68]. The ultrasound velocity v_0 of the porous substrate is given as $v_0 = \sqrt{c/\rho_{\text{sub}}}$, where c is the elastic modulus and ρ_{sub} is an effective mass density. ρ_{sub} is the sum of the mass density of the substrate and the amount of the adsorbed helium atoms which are localized on the substrate or the normal fluid with the viscosity as large as the bulk liquids. When $\Delta\rho$ of the helium adatoms are decoupled from the ultrasound motion of the substrate, the sound velocity is changed as $\Delta v/v_0 = \Delta\rho/2\rho_{\text{sub}}$.

The ultrasound measurement at 10 MHz was done for ^{4}He and ^{3}He adsorbed in Hectorite [69]. The helium properties in the 2D nanopores are well understood, as described in Sects. 3 and 4.2. At the lower coverages than 24.7 μmol/m^2, no quantum fluid state is expected for the ^{4}He adatoms from the heat capacity measurement. At the low ^{4}He coverages, the velocity change $\Delta v/v_0$ and the excess attenuation $\Delta\alpha$

of the sound propagation related to the velocity change were observed as shown in Fig. 21(a), where the vertical values are shifted appropriately. The result obviously indicates the velocity change $\Delta v/v_0$ of the order of 0.2% at the lowest temperature 50 mK. This indicates the decoupling or slippage of the ^{4}He adatoms $\Delta\rho$ for the sound propagation at 10 MHz. The mid-temperature T^* of the velocity change was defined as shown by the arrow. The coverage dependence of T^* is shown in Fig. 21(b). At higher coverages, the velocity change by the superfluid onset was observed, which agrees with that measured by the torsional oscillator [21]. Slippage of the ^{3}He adatoms was also observed at the low coverages as shown in Fig. 21(b).

Assuming a characteristic relaxation time τ obeying the Arrhenius relation: $\tau = \tau_0 \exp(E/k_B T)$, the velocity change is fitted to the equation given by $\frac{\Delta v}{v_0} = \frac{\Delta\rho^0}{2\rho_{\text{sub}}}(\frac{\omega^2\tau^2}{1+\omega^2\tau^2} - 1)$. The midpoint of the velocity change at T^* is under the condition $\omega\tau \sim 1$. Using the Kramers-Kronig relation, the excess attenuation is described as $\Delta\alpha = \frac{\Delta\rho^0\omega}{2\rho_{\text{sub}}v_0}\frac{\omega\tau}{1+\omega^2\tau^2}$. The fitting results are shown by the solid curves in Fig. 21(a). Except for the deviation of $\Delta\alpha$ above T^*, both curves are well fitted to the data. At the lowest coverage n =18.3 μmol/m^2 of ^{4}He, $\Delta\rho^0$ is about 1/3 of the ^{4}He amount adsorbed. Assuming the decoupling ratio $(1-\chi)$ to be 1/3, almost all of the ^{4}He adatoms slip or decouple below T^*. The relaxation time τ is described by $\tau_0 \approx 10^{-9}$ sec and $E/k_B \approx 5$ K [69]. τ determines the magnitude of the frictional force at the nano-scale given by $F_f = -\frac{\sigma}{\tau}V$, where V is the sliding speed. At sufficiently lower temperatures than T^* ($\tau \to \infty$), the adatoms slip (decouple) without the frictional force. $\Delta\rho^0$ and E/k_B decrease with increasing coverage, and the slippage disappears when the superfluid is observed (Fig. 21(b)).

Thus, the extremely high frequency measurements revealed the new dynamic properties of the helium adatoms in addition to the superfluidity. Slippage of ^{4}He and ^{3}He adatoms was observed also on the substrate of the graphite [70].

8 Conclusion

Using the nanopores, we have developed new paradigms of zero-D and 1D states of the ^{4}He and ^{3}He fluid films. The superfluid onsets (transitions) of the ^{4}He fluid films formed in the 1D and 3D nanopores are found to have explicit dependence on the 1D and 3D pore connections. The ^{4}He films in the 3D nanopores show the 3D superfluid transition with properties which have the common characters of the Bose-Einstein condensate to those of the 3D atomic gas. A nearly noninteracting gas state of the ^{3}He films is realized in the ^{4}He-preplated 1D and 3D nanopores. The ^{3}He nanotubes of the Boltzmann gas in the 1D pores show the dimensional crossover from 2D to 1D with decreasing temperature, followed by the degenerate state in the 1D condition. Extremely high frequency measurements for the superfluidity and dynamic properties of the adsorbed helium revealed the microscopic properties of the superfluid vortices of the ^{4}He films and nano-tribology of the adatoms.

Acknowledgements The authors thank T. Kurokawa for technical assistance. This research was partly supported by Grants-in-Aid for Scientific Research (Grant Nos. 17071006 and 17204029) from the Ministry of Education, Culture, Sports, Science and Technology of Japan.

References

1. S. Nakajima, Prog. Theor. Phys. **50**, 1101 (1973)
2. D.J. Bishop, J.D. Reppy, Phys. Rev. Lett. **40**, 1727 (1978)
3. D.J. Thouless, *Topological Quantum Numbers in Nonrelativistic Physics* (World Scientific, Singapore 1998)
4. M. Ogura, H. Namaizawa, J. Phys. Soc. Jpn. **66**, 3706 (1997)
5. M. Neumann, J. Nyeki, B. Cowan, J. Saunders, Science **317**, 1356 (2007)
6. N. Wada, M.W. Cole, J. Phys. Soc. Jpn. **77**, 111012 (2008)
7. J.D. Reppy, J. Low Temp. Phys. **87**, 205 (1992)
8. R. Toda, M. Hieda, T. Matsushita, N. Wada, J. Taniguchi, H. Ikegami, S. Inagaki, Y. Fukushima, Phys. Rev. Lett. **99**, 255301 (2007)
9. H. Fukuyama, J. Phys. Soc. Jpn. **77**, 111013 (2008)
10. S.Q. Murphy, J.D. Reppy, Physica B **165–166**, 547 (1990)
11. M.H.W. Chan, K.I. Blum, S.Q. Murphy, G.K.S. Wong, J.D. Reppy, Phys. Rev. Lett. **61**, 1950 (1988)
12. M.P.A. Fisher, P.B. Weichman, G. Grinstein, D.S. Fisher, Phys. Rev. B **40**, 546 (1989)
13. Http://www.iza-structure.org/databases/
14. T. Takaishi, Pure Appl. Chem. **58**, 1375 (1986)
15. H. Kato, N. Wada, T. Ito, S. Takayanagi, T. Watanabe, J. Phys. Soc. Jpn. **55**, 246 (1986)
16. K. Torii, T. Iwasaki, Chem. Lett. **12**, 2021 (1986)
17. T. Yanagisawa, T. Shimizu, K. Kuroda, C. Kato, Bull. Chem. Soc. Jpn. **63**, 1535 (1990)
18. S. Inagaki, Y. Fukushima, K. Kuroda, J. Chem. Soc.-Chem. Commun. **8**, 680 (1993)
19. C. Kresge, M.E. Leonowicz, W.J. Roth, J.C. Vartuli, J.S. Beck, Nature **359**, 710 (1992)
20. S. Inagaki, S. Guan, Y. Fukushima, T. Ohsuna, O. Terasaki, J. Am. Chem. Soc. **121**, 9611 (1999)
21. N. Wada, A. Inoue, H. Yano, K. Torii, Phys. Rev. B **52**, 1167 (1995)
22. E.P. Barrett, L.G. Joyner, P.P. Halenda, J. Am. Chem. Soc. **73**, 373 (1951)
23. S. Inagaki, Private communication
24. L.W. Bruch, M.W. Cole, E. Zaremba, *Physical Adsorption Forces and Phenomena* (Dover, Mineola, 2007)
25. N. Wada, Y. Yamamoto, H. Kato, T. Ito, T. Watanabe, *New Developments in Zeolite Science Technology*, ed. by Y. Murakami, A. Iijima, J.W. Ward (Kodansha, Tokyo, 1986), pp. 625–632
26. N. Wada, H. Kato, T. Watanabe, J. Low Temp. Phys. **95**, 507 (1994)
27. J. Taniguchi, A. Yamaguchi, H. Ishimoto, H. Ikegami, T. Matsushita, N. Wada, S.M. Gatica, M.W. Cole, F. Ancilotto, S. Inagaki, Y. Fukushima, Phys. Rev. Lett. **94**, 065301 (2005)
28. R. Toda, J. Taniguchi, R. Asano, T. Matsushita, N. Wada, J. Low Temp. Phys. **138**, 177 (2005)
29. H. Ikegami, T. Okuno, Y. Yamato, J. Taniguchi, N. Wada, S. Inagaki, Y. Fukushima, Phys. Rev. B **68**, 092501 (2003)
30. R. Asano, R. Toda, Y. Matsushita, M. Hieda, T. Matsushita, N. Wada, AIP Conf. Proc. **850**, 299 (2006)
31. N. Wada, K. Ishioh, T. Watanabe, J. Phys. Soc. Jpn. **61**, 931 (1992)
32. T. Matsushita, R. Toda, M. Hieda, N. Wada, J. Phys.: Conf. Ser. **150**, 032055 (2009)
33. T. Matsushita, R. Toda, M. Hieda, N. Wada, J. Low Temp. Phys. (submitted)
34. M. Morishita, T. Takagi, Phys. Rev. Lett. **87**, 185301 (2001)
35. V. Apaja, E. Krotscheck, Phys. Rev. B **64**, 134503 (2001)
36. B.E. Clements, H. Godfrin, E. Krotscheck, H.J. Lauter, P. Leiderer, V. Passiouk, C.J. Tymczak, Phys. Rev. B **53**, 12242 (1996)
37. N. Wada, H. Yano, M. Ogura, H. Namaizawa, Y. Karaki, J. Low Temp. Phys. **110**, 357 (1998)
38. S. Blundell, *Magnetism in Condensed Matter* (Oxford University Press, Oxford, 2001)
39. Y. Matsushita, J. Taniguchi, R. Toda, H. Ikegami, T. Matsushita, M. Hieda, N. Wada, J. Low Temp. Phys. **150**, 342 (2008)
40. R. Toda, Ph.D. thesis, Nagoya University, 2007
41. F. London, *Superfluids II* (Dover, New York, 1960)

42. N. Wada, R. Toda, M. Hieda, T. Matsushita, J. Phys.: Conf. Ser. **150**, 032118 (2009)
43. K. Yamashita, D.S. Hirashima, Phys. Rev. B **79**, 014501 (2009)
44. M. Bijlsma, H.T.C. Stoof, Phys. Rev. A **54**, 5085 (1996)
45. N. Wada, J. Taniguchi, H. Ikegami, S. Inagaki, Y. Fukushima, Phys. Rev. Lett. **86**, 4322 (2001)
46. T. Matsushita, R. Toda, J. Taniguchi, H. Ikegami, N. Wada, J. Low Temp. Phys. **138**(1–2), 289 (2005) (Sp. Iss. SI)
47. N. Wada, H. Yano, Y. Karaki, J. Low Temp. Phys. **113**, 317 (1998)
48. W. Saam, M. Cole, Phys. Rev. B **11**, 1086 (1975)
49. M.W. Cole, F. Ancilotto, S.M. Gatica, J. Low Temp. Phys. **138**, 195 (2005)
50. Y. Okaue, Y. Saiga, D.S. Hirashima, J. Phys. Soc. Jpn. **75**, 053603 (2006)
51. H.Y. Kim, S.M. Gatica, M.W. Cole, J. Phys. Chem. A **111**, 12439 (2007)
52. B. Bhattacharyya, F.M. Gasparini, Phys. Rev. Lett. **49**, 919 (1982)
53. B. Bhattacharyya, F. Gasparini, Phys. Rev. B **31**, 2719 (1985)
54. M. Aichinger, S. Kilić, E. Krotscheck, L. Vranješ, Phys. Rev. B **70**, 155412 (2004)
55. R. Toda, Y. Matsushita, M. Hieda, T. Matsushita, N. Wada, J. Low Temp. Phys. **148**, 785 (2007)
56. M. Kim, W.I. Glaberson, Phys. Rev. Lett. **52**, 53 (1984)
57. K. Gillis, S. Volz, J. Mochel, Phys. Rev. B **40**, 6684 (1989)
58. D. Finotello, Y.Y. Yu, F.M. Gasparini, Phys. Rev. B **41**, 10994 (1990)
59. D. Finotello, F.M. Gasparini, Phys. Rev. Lett. **55**, 2156 (1985)
60. G. Agnolet, D.F. McQueeney, J.D. Reppy, Phys. Rev. B **39**, 8934 (1989)
61. H. Cho, G.A. Williams, Phys. Rev. Lett. **75**, 1562 (1995)
62. M. Hieda, K. Matsuda, T. Kato, T. Matsushita, N. Wada, J. Phys. Soc. Jpn. **78**, 033604 (2009)
63. V. Ambegaokar, B.I. Halperin, D.R. Nelson, E.D. Siggia, Phys. Rev. Lett. **40**, 783 (1978)
64. M. Oda, R. Hieda, T. Toda, N. Matsushita, N. Wada, J. Low Temp. Phys. (submitted)
65. E. Kim, M.H.W. Chan, Nature **427**, 225 (2004)
66. J. Krim, D.H. Solina, R. Chiarello, Phys. Rev. Lett. **66**, 181 (1991)
67. C. Daly, J. Krim, Phys. Rev. Lett. **76**, 803 (1996)
68. N. Mulders, J.R. Beamish, Phys. Rev. Lett. **62**, 438 (1989)
69. M. Hieda, T. Nishino, M. Suzuki, N. Wada, K. Torii, Phys. Rev. Lett. **85**, 5142 (2000)
70. N. Hosomi, A. Tanabe, M. Suzuki, M. Hieda, Phys. Rev. B **75**, 064513 (2007)